Faculty of Physics and Astronomy

University of Heidelberg

Diploma thesis

in Physics

submitted by

Arne Fischer

born in Heidelberg

April 2009

Laser Spectroscopy on the Negative Osmium Ion

This diploma thesis was carried out by Arne Fischer at the
Max Planck Institute for Nuclear Physics
under the supervision of
Priv.-Doz. Dr. Alban Kellerbauer

Laserspektroskopie am negativen Osmiumion:

1999 wurde im negativen Osmiumion ein elektrischer Dipolübergang gefunden. Es ist der einzige bekannte erlaubte Übergang in einem atomaren Anion. Das Ziel der vorliegenden Diplomarbeit war es, diesen Übergang in den verschiedenen Osmiumisotopen mittels kollinearer Laserspektroskopie genauer zu untersuchen. In solch einem Aufbau werden der Spektroskopielaser und der Ionenstrahl im Ultrahochvakuum parallel überlagert. Voraussetzung für die Messungen war die Entwicklung einer sensitiven Nachweismethode. Sie basiert auf resonanter Anregung der negativen Ionen mit dem Spektroskopielaser gefolgt von Neutralisation in einem starken elektrischen Feld. Die durchgeführte experimentelle Arbeit beinhaltet Messungen der Frequenz des Dipolübergangs in allen natürlich vorkommenden Osmiumisotopen und des Wirkungsquerschnitts des Übergangs in $^{192}Os^-$. Die Messgenauigkeit reichte aus um die Hyperfeinstruktur von $^{187}Os^-$ und $^{189}Os^-$ aufzulösen, was zu neuen Erkenntnissen über den Drehimpuls des angeregten Zustands führte. Die experimentelle Arbeit und der Aufbau des Experiments werden hier vorgestellt und die Ergebnisse der Spektroskopie mit früheren experimentellen Ergebnissen und theoretischen Berechnungen verglichen.

Laser Spectroscopy on the Negative Osmium Ion:

In 1999 an electric-dipole transition was found in the negative osmium ion, so far the only known allowed transition in an atomic anion. The objective of this diploma thesis was to study the transition in the different isotopes of negative osmium by collinear laser spectroscopy. In such a setup the laser beam is superimposed with an ion beam propagating in parallel in an ultra-high vacuum. For the spectroscopy measurement an innovative detection scheme was developed, which is based on resonant laser excitation followed by neutralization in a strong electric field. The experimental survey included measurements of the electric-dipole transition frequency in all naturally occurring osmium isotopes as well as the absorption cross-section in $^{192}Os^-$. The hyperfine structure of the transition in $^{187}Os^-$ and $^{189}Os^-$ was resolved, yielding previously unknown information on the angular momentum of the excited state. The experimental technique and setup are presented, and the results of the spectroscopy are compared with prior experimental data and theoretical calculations.

CONTENTS

LIST OF FIGURES

1. INTRODUCTION

In negative ions the attractive potential of the nucleus is strongly suppressed. Hence at first view their formation doesn't seem to be favorable. Nevertheless nearly every element forms a negative ion due to polarization and electron–electron correlation effects. The excess electron in the electron shell causes all other electrons to adjust their motions in order to minimize the overlap of their wavefunctions in accordance with the Pauli exclusion principle (exchange correlation) and electrostatic repulsion (Coulomb correlation). Thereby the whole system gains potential energy. If one of the electrons is highly excited the correlation effects are reduced and it essentially moves around a neutral atomic core without much attractive potential. Therefore excited bound states are rare in negative ions. In addition it was found that most of them have the same parity as the ground state, which means that transitions between them are forbidden and consequently have low cross sections.

In 1999 the first excited bound state of a negative ion with opposite parity relative to the ground state was found in the transition metal osmium. It was deduced from the measured transition strength that this transition is an electric dipole transition, which makes negative osmium accessible to standard atomic-physics methods such as laser cooling and laser spectroscopy.

Our UNIC project (Ultracold Negative Ions by indirect laser Cooling) at the Max Planck Institute for Nuclear Physics in Heidelberg has the aim to demonstrate laser cooling of the negative osmium ion. The lowest temperature achievable with laser cooling is the Doppler limit, which is proportional to the natural linewidth of the transition. Having established laser cooling of negative ions, the cold ions could be used to sympathetically cool other negative particles. For sympathetic cooling the already cold particles and the ones to be cooled are brought together in the same ion trap. The warm particles then lose their kinetic energy via Coulomb collisions with the cold ones until they are thermalized. Hence this cooling technique would allow precision studies on any negatively charged ions, such as subatomic particles or even molecules.

For the laser cooling a good knowledge of the cooling transition is necessary. Therefore a first experimental milestone was the precision spectroscopy of the cooling transition. Osmium has seven naturally occurring isotopes. The one with the highest natural abundance is $^{192}Os^-$, which was therefore chosen as the prime candidate for the laser cooling experiment. For efficient laser cooling especially the wavelength of the cooling transition and its cross section are of great interest. Among the osmium isotopes are also two with odd mass numbers, $^{187}Os^-$ and $^{189}Os^-$, which have a non-vanishing nuclear spin. There-

fore the dipole transition in these isotopes exhibits a hyperfine splitting. Another effect which can be studied if several isotopes of an element are available for spectroscopy is the isotope shift. Both the hyperfine structure and the isotope shift provide information on the electron wavefunction of the system and are therefore of interest.

The goal of this diploma thesis was to perform laser spectroscopy on a negative osmium ion beam. The spectroscopy was performed in a collinear setup, where the spectroscopy laser and the ion beam are superimposed collinearly. For the measurement an effective detection scheme had to be developed and a spectrometer based on this scheme had to be designed. In addition the laser system for the spectroscopy had to be put into operation and optimized. The spectroscopic survey included measurements of:

- the frequency of the dipole transition in $^{192}Os^-$ and its cross section;
- the hyperfine structure of the dipole transition in $^{187}Os^-$ and $^{189}Os^-$;
- the isotope shift of the dipole transition in all naturally occurring isotopes of Os^-.

The experimental setup, the theoretical framework, and the results of the spectroscopy are presented in this thesis.

2. THE NEGATIVE OSMIUM ION

2.1 Atomic anions

In a neutral atom the electrons are bound to the nucleus by Coulomb interaction. This gives rise to a long-ranged potential and an infinite number of bound states. Seen from a distance the positive charge of the nucleus is shielded by the negatively charged electrons and an approaching electron experiences no attractive Coulomb potential. Therefore, from this point of view, the formation of negative ions should not be favorable. But actually nearly every element is able to form a negative ion. The energy gained by the atom due to the formation of a negative ion (the binding energy of the negative ion) is also called the electron affinity (Fig. 2.1). In the majority of cases it is of the order of 1 eV, which means that the binding energy of the additional electron in a negative ion is roughly one order of magnitude smaller than the binding energy of the valence electron in neutral atoms. In hydrogen, for example, the binding energy of the electrons forming the negative ion is only 0.75 eV, compared with 13.6 eV for the neutral atom. A distinctive feature of negative ions is that, in contrast to neutral atoms and positive ions, they possess either no bound states

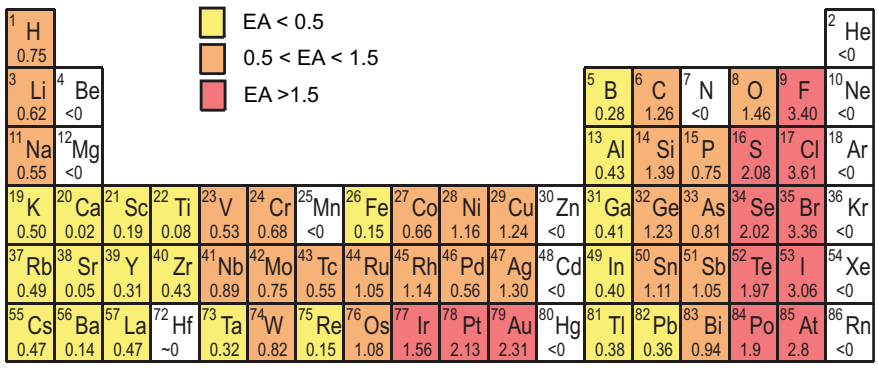

Fig. 2.1: Periodic table of the elements. The number below the symbol of each atom is its electron affinity (EA). It is the energy an atom gains by forming a negative ion or simply the binding energy of the extra electron in a negative ion. The EA values are taken from [1].

at all or only a limited number of them [2]. In addition these bound states belong in almost every case to the same fine structure multiplet, which means that they have the same parity. Thus electric-dipole (E1) transitions between such states are forbidden and therefore not useful for optical spectroscopy (due to extremely low cross sections). Actually there is only one known element whose negative ion exhibits an excited bound state with opposite parity relative to the ground state, which is osmium. The characteristics of the negative osmium ion will be discussed in more detail in the following section. Theoretical calculations predicted bound–bound E1-transitions also in the negative ions of some lanthanides and actinides [3, 4, 5, 6] as well as for cesium [7, 8, 9], but for cesium and lanthanum their existence was later ruled out experimentally [10, 11].

The formation of negative ions can be rationalized in the following way. An electron coming close to an atom polarizes its electron shell and thereby induces a dipole potential, by which the electron is attracted. This potential is weak and has a $1/r^4$ dependence making it short ranged in comparison to the $1/r$ dependent Coulomb potential. However, for quantitative predictions about binding energies in negative ions this explanation is not sufficient.

A quantum mechanical approach is to explain negative ions on the basis of electron–electron correlation effects. Due to the extra electron in the electron shell all electrons adjust their radial and angular states to minimize the overlap of their wavefunctions, and therefore minimize the total energy of the newly bound system. A good example are the halogens: if they attract an additional electron they gain a closed shell structure that corresponds to the energetically advantageous noble gas configuration. Hence their electron affinity is the highest of all elements. Exactly the opposite is true for noble gases. They already have a closed shell structure and an additional electron would require a new electron shell, which is energetically disadvantageous. Therefore noble gases have a negative electron affinity and form no stable negative ions. Correlation effects can also explain why there are not infinite series of Rydberg states in negative ions, as there are in neutral atoms. In Rydberg states the excited electrons have a high spatial probability density far away from the nucleus. In a negative ion this means that the correlation effects get smaller and the additional electron starts seeing simply a neutral atom without any attractive potential.

2.2 Discovery of a bound excited state in Os^-

Almost ten years ago, the first excited bound state of a negative ion with opposite parity relative to the ground state was found in the transition metal osmium [12]. In that experiment a pulsed dye laser was used in a transverse configuration [11] for laser photo detachment spectroscopy (see Chap. 3) on the negative osmium ion $^{192}Os^-$. Figure 2.2 shows the photo detachment spectrum from Ref. [12].

The weaker resonance at $\lambda = 1162.734(2)$ is due to a two-photon detachment process, in

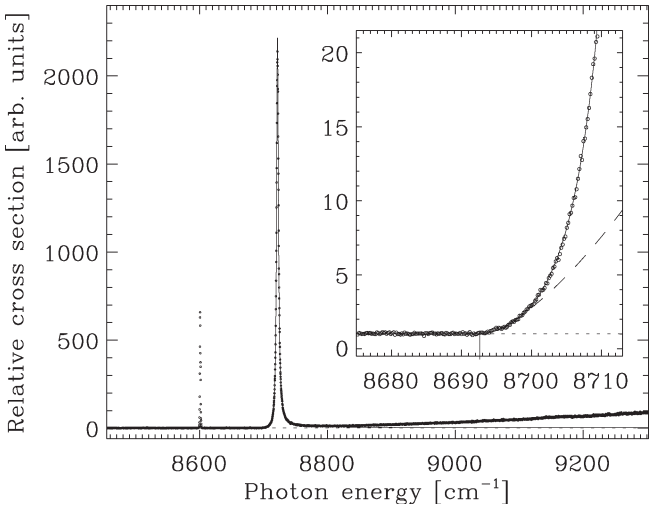

Fig. 2.2: Resonances found in the negative osmium ion. The stronger resonance is slightly above the threshold, which can be identified due to the rising signal on the right side. The inset shows a high-resolution scan around the threshold (Fig. 2 of Ref. [12]).

which the first photon resonantly excites the ion into the J_{e1} state (relevant E1 transition) whereas a second photon leads to the detachment. The strong resonance at $\lambda = 1146.600(4)$ is due to a resonant excitation into the auto-detachment state J_{e2}. The slow rising signal to higher photon energies was explained by above-threshold detachment from the ground state $^4F_{9/2}$. An analysis led to a threshold position of 1.07780(12) eV. These experimental results and theoretical calculations on the ground state configuration [13], resulted in the energy level diagram shown in Fig. 2.3. The ground state of $^{192}Os^-$ belongs to a fine-structure multiplet with four components. The excited state is only slightly bound with 11.48(12) meV. The cross section of the resonant E1 transition from $^4F_{9/2}$ to $^6D_{J_{e1}}$ was found to be of the order of 10^{-16} cm^2, which is small for a fully allowed electric dipole transition. But since the transition is spin forbidden ($\Delta S = +1$) this value lies in the expected range for such transitions in heavy elements. The cross section for photo-detachment from the excited $^6D_{J_{e1}}$ state was found to be of the order of 10^{-17} cm^2.

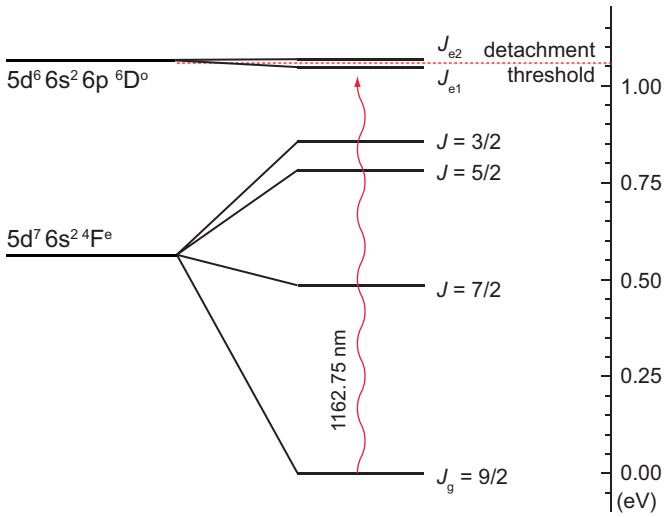

Fig. 2.3: Energy level diagram of the negative osmium ion. The lowest level is the $^4F_{9/2}$ ground state, which is bound by 1.08 eV and belongs to a fine structure multiplet, which includes also states with $J = 7/2$, $5/2$ and $3/2$. Near the threshold lies another multiplet consisting of a $^6D_{J_{e1}}$ state which is slightly bound by 11 meV and a second, unbound $^6D_{J_{e2}}$ state, which is 4 meV above the threshold.

3. COLLINEAR DETACHMENT SPECTROSCOPY

Laser spectroscopy on a low-energy beam of atoms or ions can be performed using one of two basic geometries. First a transverse one, where the spectroscopy laser beam crosses the ion beam under a 90° angle and second a collinear one, where the laser and the ion beam are parallel superimposed in the interaction region. The collinear setup has two advantages in comparison to the transverse one:

- A much longer interaction region (in a transverse setup the length is limited by the diameter of the laser beam), yielding a stronger signal;
- The so called velocity bunching, where the Doppler broadening is reduced at higher beam energies (see Sec. 3.2).

Therefore the collinear setup was chosen for the experiment. For signal detection there are again several possibilities, such as detection of fluorescence light, absorption and detachment spectroscopy. The disadvantage of fluorescence light detection with a photomultiplier is that the photomultiplier can only cover a relatively small solid angle and especially not the whole interaction region of the collinear setup. The disadvantage of absorption spectroscopy would be that the density in an ion beam is low and the fraction of absorbed light would be very small. Therefore detachment spectroscopy was chosen for the experiment. Here the spectroscopy laser neutralizes the ions. Since the detection of the loss of a very small number of ions out of roughly 10^{10} would be extremely difficult, the appearance of neutral particles is instead detected with a micro-channel plate detector (MCP).

3.1 Measurement principle

The experiment was designed as a photo-detachment setup, where the measured signal is caused by the neutralization of ions. To measure the frequency of a bound–bound transition in Os^- a two step process is necessary, namely excitation and neutralization. Excitation and neutralization of Os^- can both be induced by photons of the laser beam. However, since the electron in the excited state is only slightly bound with 11 meV, other detachment processes are also possible, such as black-body radiation, collisions with residual gas atoms and interactions with electric fields.

Assuming equal cross sections for the resonant excitation and detachment steps, the measured signal depends on the square of the laser intensity. Since the used cw OPO

laser system (see Sec. 3.5) has a relatively low output power of only 200 mW the resulting signal would be very weak. Moreover, the cross section for neutralization (10^{-17} cm^2) was measured to be roughly one order of magnitude smaller than the resonant excitation cross section (10^{-16} cm^2) [12], such that the transition rate is limited by the detachment rate. Therefore other detachment processes might be used to improve the signal.

A part of the black-body spectrum has in principle enough energy to neutralize excited ions, but since the intensity is small compared to the laserpower the detachment due to thermal photons can be neglected. Collisions with residual gas atoms could in principle also cause neutralization, but the collision energies at a typical beam energy of 5 keV are high enough to also detach electrons from the ground state. This could lead to a disturbing background signal, that has to be reduced by a good vacuum. The cross sections for collisions between gas atoms/molecules and negative ions with energies of some keV are of the order of 10^{-15} cm^{-2} [14, 15, 16, 17]. In the vacuum which is present in the spectroscopy part of the apparatus (10^{-9} mbar) this leads to a mean free path l of roughly 10^5 m:

$$l \approx (n\sigma)^{-1}\,, \tag{3.1}$$

where n is the particle density and σ the cross section. Therefore detachment due to collisions can also be neglected.

In external static electric fields of strengths F, the rate of detachment W of excited negative ions can be estimated by [14]:

$$W = B^2 \frac{(2L+1)}{2\gamma^{M_L}} \frac{M_L!\,(L+M_L)!}{(L-M_L)!} \left(\frac{2\gamma^2}{F}\right)^{\frac{2Z_{\text{eff}}}{\gamma}-M_L-1} e^{-\frac{2\gamma^3}{3F}} \tag{3.2}$$

where B is determined by the electron wavefunction, γ is related to the binding energy E_B via $\gamma = (-2E_B)^{1/2}$, Z_{eff} is the effective charge of the nucleus, L is the orbital angular momentum and M_L its projection. The lifetime of an excited ion in an electric field is then $1/W$. For the excited ^{6}D state in osmium ($Z = 0$, $L = 2$, $E_B = 11.5$ meV, $B = 0.1$ and $M_L = 2$ [18]) the breakup lifetime is of the order of 1 s for an electric field of $0.3{\times}10^6$ Vm^{-1} and below 1 μs for $F = 10^6$ Vm^{-1}.

Therefore it is possible to induce the detachment step in a strong electric field. To use this effect, an ionizer was installed at the end of the interaction region. It neutralizes excited ions in an electric field of up to $2{\times}10^6$Vm^{-1} and reduces the two photon process (excitation and neutralization) to a one photon process (excitation only), which only depends in a linear way on the laser power. But in any case the ion has to be excited before the detachment of the electron. The easiest way to improve the fraction of ions being excited is to use a long interaction region. Hence the experiment was designed with a long (500 mm) interaction region.

3.2 Collinear spectroscopy

In optical spectroscopy the resolution is often limited by the Doppler broadening of spectral lines. Due to the thermal motion of atoms and molecules the transition frequency of the single particle is Doppler shifted, which leads to a line broadening for a many-particle system with slightly different velocities. A technique which reduces this effect is collinear spectroscopy in a fast ion beam, which was first described by Kaufmann in 1976 [19]. It uses the so called velocity bunching phenomenon. If an ion beam is accelerated the velocity distribution of the particles in the beam in forward direction is successively compressed with increasing kinetic energy. In a collinear setup, this leads to a reduced Doppler broadening.

In a collinear setup the resonance frequency ν' of a transition is Doppler shifted with respect to the frequency at rest ν_0. To first order the resulting frequency is given by:

$$\nu' = \nu_0 \left(1 + \frac{v}{c}\right) \tag{3.3}$$

where v is the velocity of the atoms. Using $v = \sqrt{\frac{2E}{m}}$ (non-relativistic) in Eq. 3.3 one finds:

$$\nu' = \nu_0 \left(1 + \frac{1}{c}\sqrt{\frac{2E}{m}}\right) \tag{3.4}$$

and for its derivative with respect to the particle energy E:

$$\frac{d\nu'}{dE} = \frac{1}{m}\frac{\nu_0}{c}\sqrt{\frac{m}{2E}} \tag{3.5}$$

which means that:

$$d\nu' \propto \frac{1}{\sqrt{E}}\, dE \tag{3.6}$$

From Eq. (3.6) follows that for higher beam energies the energy distribution ΔE results in a smaller frequency distribution $\Delta\nu'$ than for low ones (Fig. 3.1). This explains the velocity bunching effect mentioned above. It means that the Doppler broadening can be reduced even below the natural line width if the beam energy is chosen high enough and that it is no longer a limiting factor for the precision. In this experiment typical beam energies are of the order of 5 keV. This results in a reduction of the Doppler broadening of about a factor of 10 for the collinear setup compared to the transverse one. Another desirable aspect of the collinear setup is the long interaction region, as mentioned before. This makes it easier to also observe transitions with low cross sections.

3.3 Ion beamline

The collinear spectroscopy setup is shown in Fig. 3.2. The ions are produced in a Middleton-

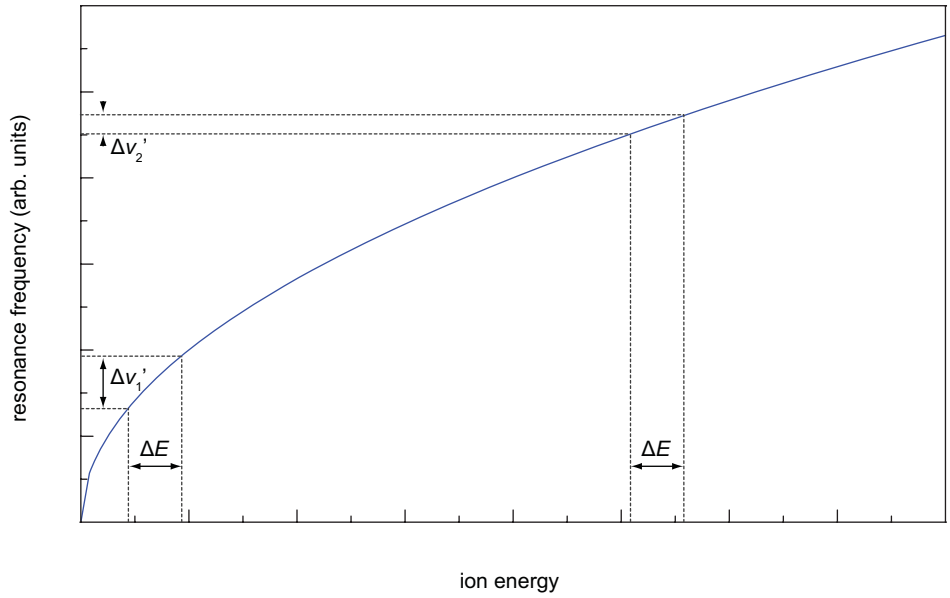

Fig. 3.1: Relation between the ion energy and the Doppler-shifted resonance frequency. The blue line is the plot of Eq. (3.4). The higher the ion energy E the smaller is the frequency broadening $\Delta\nu'$ due to the same energy distribution ΔE of the ions.

type negative-ion sputter source (MISS) [20]. It is able to produce an ion beam of some hundred nA with energies from 1 to 6.5 keV. The source is set to a potential of up to -6.5 kV and is therefore mounted in a high voltage cage and controlled via an optical USB extension. In the center of the source is a cathode with the sputter target consisting of compressed metal osmium powder (Fig. 3.3). The cathode is electrically isolated from the rest of the source and set to a potential below the source potential. A lateral cesium reservoir can be heated for evaporating caesium. Cesium vapor leaving the reservoir is positively ionized by a hot filament in front of the cathode and accelerated towards the more negative osmium target. As it hits the osmium target it sputters osmium atoms and ions and forms a thin cesium layer on the surface of the target, which enhances the fraction of produced negative ions. To support the formation of a stable cesium layer the cathode is water cooled. The ions are accelerated towards an aperture and finally extracted by a grounded extraction electrode. Since the ions are produced on the cathode and the final extraction electrode is grounded, their energy is determined by the cathode potential. The ion current is mainly controlled by the potential difference between the cathode and the rest of the source, the cesium reservoir temperature and the filament current.

Directly downstream of the source, the ion beam is focused by an electrostatic einzel lens. It consists of three ring electrodes in a row. The two outer ones are grounded and the

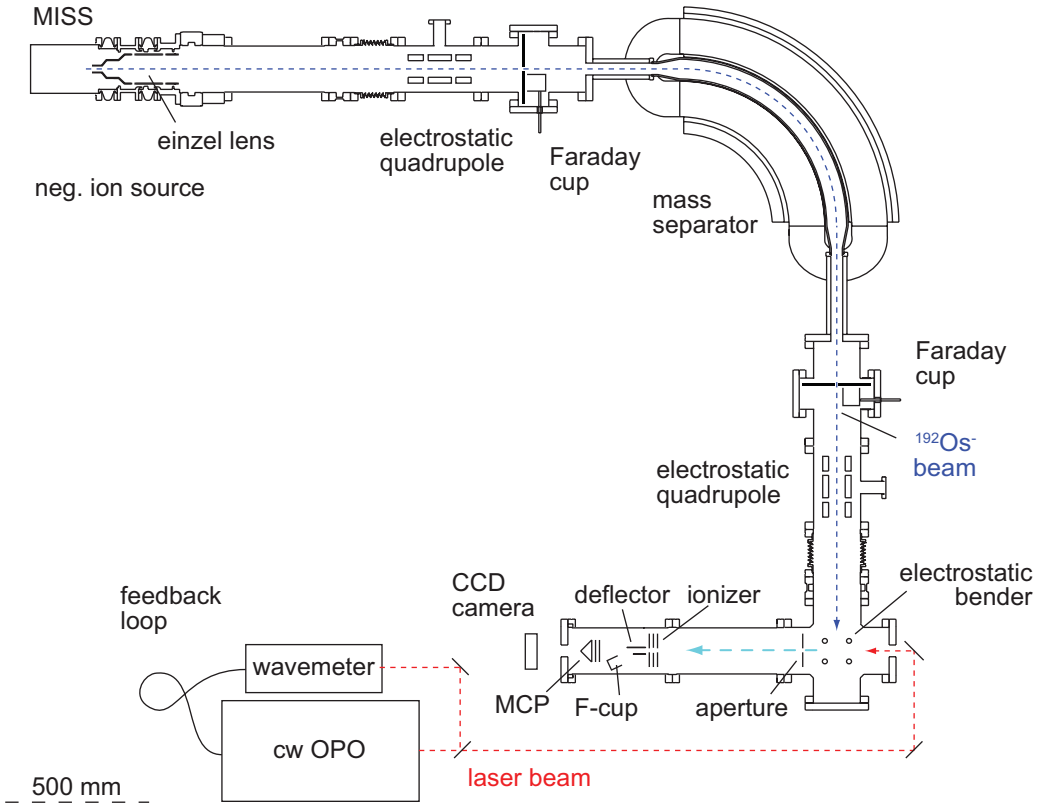

Fig. 3.2: Collinear spectroscopy setup. The beam line begins in the upper left of the figure with the MISS and ends in the bottom center with the MCP.

central one is set to a negative potential of up to −6.5 kV. After the einzel lens the beam passes an electrostatic quadrupole triplet which guides the beam and focuses it into a large (R = 500 mm) 90° dipole magnet for mass separation. To enhance the resolving power, the ion beam passes slits in front and behind the magnet. Hence the mass separation can be optimized by changing the focus of the quadrupoles and the size of the slits. Overall the system has a typical resolving power of 180. In Fig. 3.4 a scan of the magnetic field of the mass separator is shown. Before mass separation the ion beam consists of all naturally occuring osmium isotopes, other atomic ions (like H^-, O^-,..) and some molecules. By mass separation it is possible to obtain a beam which consists of over 90% of $^{192}Os^-$ with low impurities of $^{190}OsH^-$ and $^{192}OsH^-$. The source and the ion beam setup around the mass separation stage are described in more detail in [21]. The mass separator is followed by another quadrupole triplet, which is again used for refocusing, guiding and shaping the beam. Afterwards the beam is redirected by a 90° electrostatic bender. It consists of four vertically orientated hyperbolical electrodes which are shown in Fig. 3.2. To guide the

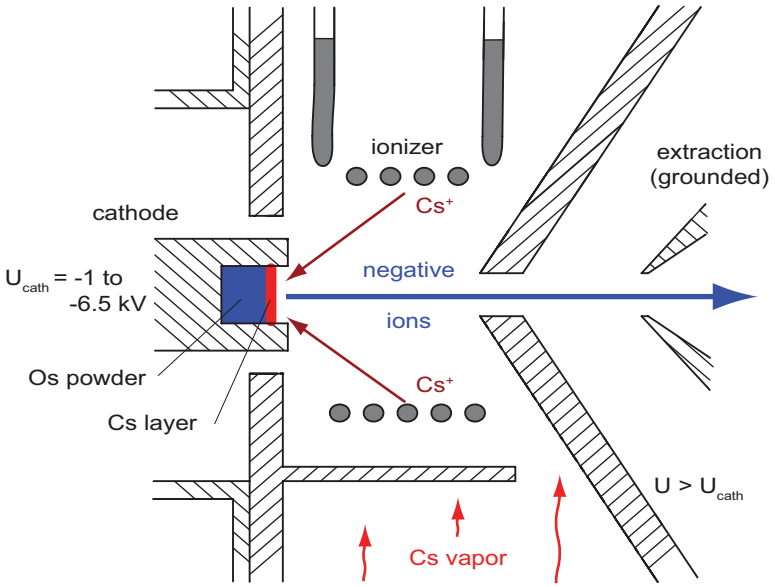

Fig. 3.3: Sketch of the ion source. On the left is the cathode with the osmium target. The produced ions are accelerated and extracted to the right. Adopted from [21].

beam to the left, the upper left electrode is set to a positive potential and the rest to a negative potential with the same magnitude. The ion beam exits the bender to the left and enters the interaction region through an entrance aperture with a diameter of 7.5 mm. The spectroscopy laser beam ($\approx$ 1 mm diameter) enters the vacuum tube from the right and is superimposed collinearly with the ion beam on a length of 520 mm. In this part of the apparatus osmium ions can be excited by the laser or neutralized by two-photon absorption. At the end of the interaction region a micro-channel plate (MCP) detects neutral particles. The MCP can be moved out of the beam axis, which permits diagnostics of the laser beam with a CCD camera (DAT TaperCamD).

For diagnostics of the ion beam three Faraday cups are installed. The first one is located after the first quadrupole triplet, the second one after the mass separation stage and the third one in the spectrometer.

The vacuum is provided by five turbo pumps, sufficient to reach 10^{-8} mbar upstream of the mass separation, 5×10^{-9} mbar downstream of it and finally below 5×10^{-9} mbar in the interaction region and the spectrometer during operation.

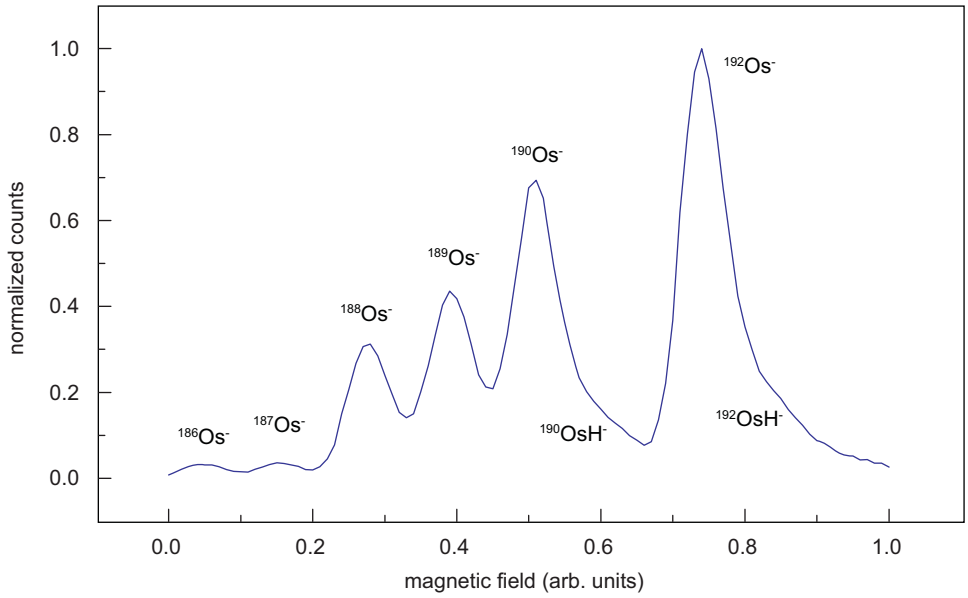

Fig. 3.4: Ion current as a function of the magnetic field of the mass separator magnet. All natural abundant osmium isotopes except $^{184}Os^-$ are observed. Its natural abundance is too low to see it in this spectrum.

3.4 Spectrometer

Fig. 3.5 shows a sketch of the spectrometer. It is located at the end of the interaction region and consists of an ionizer, a deflector, a Faraday cup for ion detection and the MCP for neutral particle detection (Fig. 3.5).

The particle beam consisting of negative ions (either in the ground or excited state) and of neutral atoms enters the spectrometer through the ionizer (light blue arrow). It consists of three concentric apertures with a diameter of 7.5 mm and spaced apart 3.5 mm. Each aperture consists of two stainless steel plates with a thickness of 0.75 mm, which are welded with a copper mesh subtended between them (transparency 70%). The two outer apertures are grounded and the central one is set to a potential of up to ± 6.5 kV. This allows to produce a maximum longitudinal electric field between the meshes of nearly $2{\times}10^6$ Vm^{-1}, which is high enough to neutralize excited ions (see Sec. 3.1).

After the ionizer the particles pass the deflector, a parallel plate capacitor whose lower plate is grounded and whose upper plate is set to a potential of roughly −1.5 kV, depending on the ion energy. Due to the electric field in the deflector the remaining ions are deflected into a Faraday-cup (blue arrow), consisting of an inner cup, which is connected to a picoampere meter (Keithley 6485) and a grounded outer cup. At this point typically

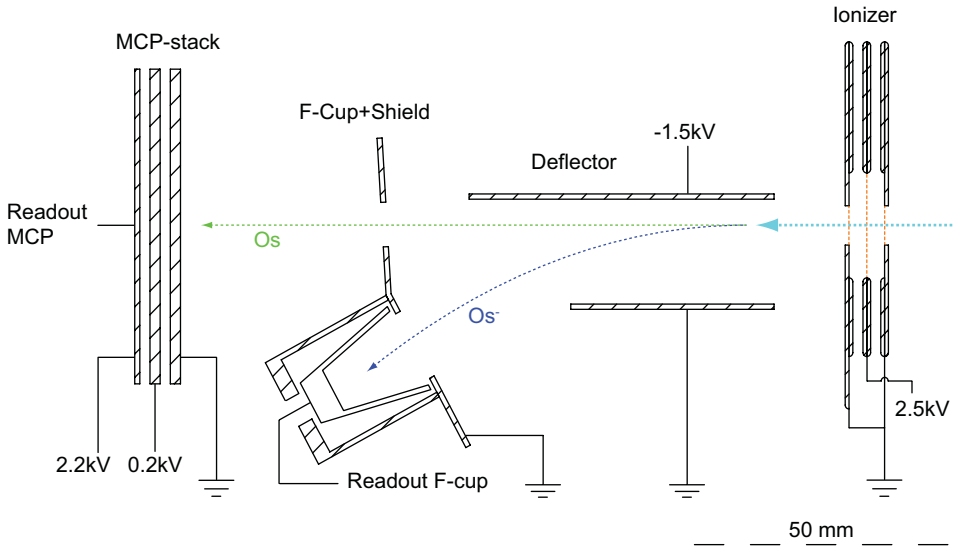

Fig. 3.5: Detailed sketch of the spectrometer. The ions and already neutralized osmium atoms enter from the right. Excited ions are neutralized in the ionizer. Afterwards remaining negative ions are deflected into the Faraday cup and neutral atoms are counted on the micro channel plate detector (MCP).

10% of the mass-separated ions arrive. The particles which were neutralized either in the ionizer or already by the laser in the interaction region traverse a shield and reach the MCP (green arrow), where they are counted with an efficiency of 30–40%. The shield has an opening of 8.5 mm, which allows the beam to pass and prevents secondary particles (e.g. produced by ions missing the Faraday-cup) from reaching the MCP.

On the MCP detector the neutral particles are detected. It consists of two micro channel plates in a chevron configuration in front of a metal readout anode. In an MCP the impacting particles produce a cascade of electrons via secondary emission. To amplify and to guide the electron avalanche to the anode the first plate is grounded, the second is on a potential of 0.2 kV and finally the anode is placed at a potential of 2.2 kV.

3.5 Laser system

The spectroscopy laser is a custom-built (Xiton Photonics) cw optical parametric oscillator system (OPO), which is pumped by a frequency-doubled Nd:YAG laser (Coherent Verdi V5). The main component of the OPO is a nonlinear crystal, which is embedded in a bow-tie cavity (Fig. 3.6). The crystal is a periodically poled lithium niobate crystal with a period of 6.92 μm. The pump beam is focused into the crystal where it is split up into

an idler and a signal wave, fulfilling energy conservation and the quasi-phase matching condition. Due to energy conservation the sum of the energies of the idler and the signal photons is the same as the one of the pump beam: $\lambda_p^{-1} = \lambda_s^{-1} + \lambda_i^{-1}$. In contrast to phase matching quasi-phase matching allows a phase mismatch over some propagation distance, but here the nonlinear interaction is reversed at positions where the conversion would otherwise take place in the wrong direction (this would mean for example, that the pump beam would gain energy from the signal and the idler beam instead of the other way around). The nonlinear interaction is reversed by changing the polarization of the nonlinear crystal. The pump beam has a wavelength of 532 nm and the resulting signal and idler wavelengths are roughly 980 nm and 1163 nm.

Since only the frequency of the idler wave is needed for the spectroscopy the resonator mirrors are high reflecting at 1163 nm making the resonator oscillate on the idler wave. The outcoupling mirror allows roughly 4% of it to be coupled out for the experiment. The resulting beam has a bandwidth $\Gamma_{\text{laser}} \leq 5$ MHz and provides up to 200 mW of infrared light at a pumping power of 2W. The threshold pump power is around 700 mW depending on the alignment of the resonator.

The laser frequency is adjusted by varying one or several of the following parameters: the temperature of the nonlinear crystal, the angle of an etalon placed in the beam and the length of the resonator cavity. Changing the crystal temperature results in a shift of the gain profile (width $\approx$ 2.4 THz). Therefore the crystal is mounted in an oven, which stabilizes the temperature and allows changes down to 0.2°K. This is sufficient for a coarse tuning of the frequency. The next finer frequency tuning step is done with a rotatable etalon embedded in the resonator. The light is reflected within the etalon, which leads to constructive or destructive interference depending on its thickness and the wavelength of the light. By changing the angle of the etalon in a small range one can vary the thickness of the etalon as seen by the light. The angle has to be small to make sure that the overlap of counter propagating waves is still sufficient for interference. The etalon used here has a thickness of 0.2 mm and a reflectivity of 40%. This results in a free spectral range of roughly 500 GHz and a bandwidth of 150 GHz. The fine tuning is finally done by changing the resonator length. For this purpose one of the resonator mirrors is actuated by a piezo. If these three steps are not sufficient to obtain the desired wavelength, a slight variation of the the pump power offers an additional possibility.

The wavelength is determined and stabilized by a wavemeter (HighFinesse WSU-30 IR), which is calibrated by a stabilized diode laser. The calibration laser is locked on the D_2 line in ^{6}Li via Doppler-free spectroscopy. A part of the laserlight is coupled into a fiber and sent to the wavemeter, which uses a PID controller connected to the actuated resonator mirror to adjust the laser frequency. In this way, continuous scans of the laser frequency over a range of 1.5 GHz are possible.

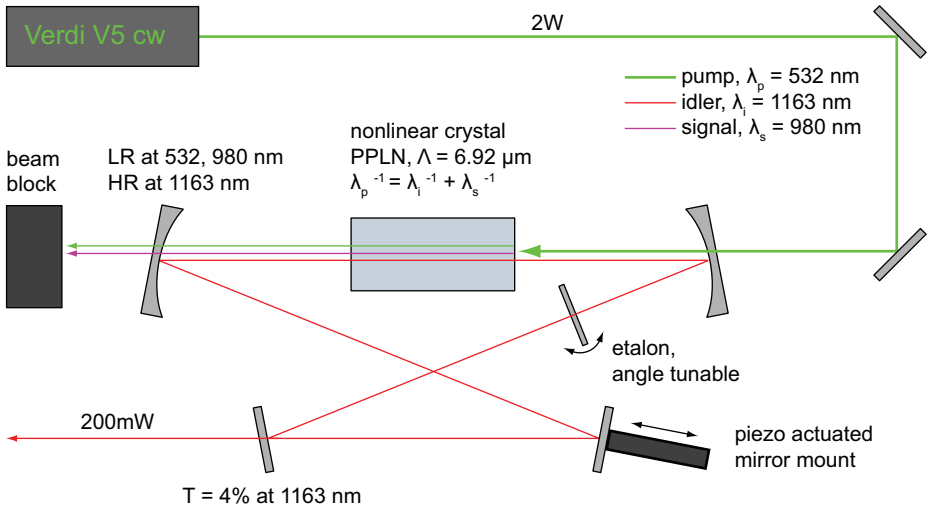

Fig. 3.6: The OPO laser system used in the experiment. Its centerpiece is a nonlinear crystal, which is embedded in a bow-tie cavity consisting of two focusing mirrors and two plane mirrors.

3.6 Data acquisition

The overall electronic setup for data acquisition is shown in Fig. 3.7. The raw signal coming from the MCP is first amplified by a preamplifier and then converted into a digital signal by a discriminator. The discriminator level is chosen such that the background signal is not higher than 10 Hz without ion beam. The threshold was further optimized for a better signal-to-noise ratio during the course of the measurement. The digital signal is recorded by a multichannel scaler card. A digital signal generator card (SpinCore PulseBlaser) acts as an external clock for the measurement and the data acquisition. It produces TTL pulses of a duration down to 50 ns at 24 independently controlled channels. For the spectroscopy only three of the channels are used. The first controls the frequency of an optical chopper (ThorLabs MC1000A), which alternatingly blocks and unblocks the laser light for the experiment. The two other channels control the counter. One is for counting with *light on* and one for counting with *light off* (Fig. 3.8). Since the chopping is done with a rotating slot blade the laser beam path is not instantaneously blocked or unblocked. Instead it always takes some time during which the beam is partly blocked, and the laser intensity recorded on a photodiode behind the chopper follows a rectangular profile with smoothed corners (see Fig. 3.9). In order to record only counts when the laser is totally blocked or unblocked the length of the readout windows ($\Delta t = 1.75$ ms) is chosen shorter than the "on" and "off" phases of the chopper ($\Delta t = 2$ ms). In order to compensate for the background noise the "off"-counts are later substracted from the "on"-counts recorded

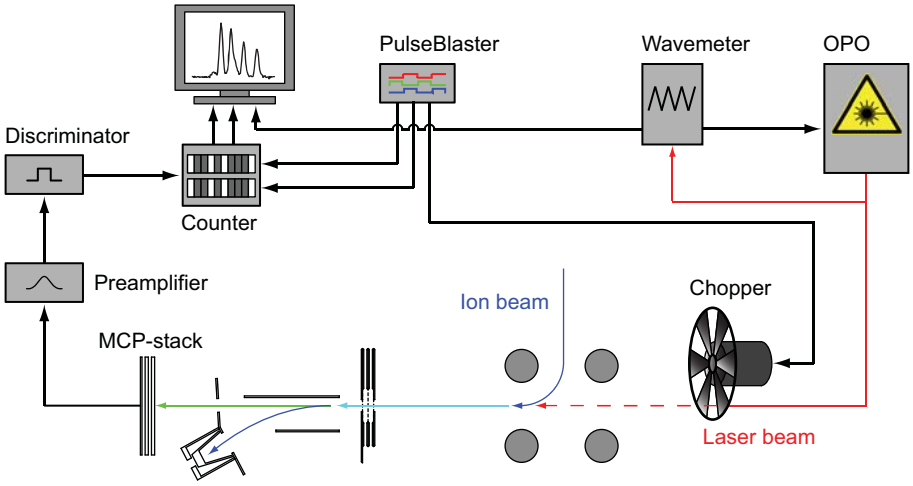

Fig. 3.7: Scheme of the electronic setup. The raw MCP signal passes first a preamplifier, than a discriminator and finally the pulses are counted. The timing of the measurement is controlled by a PulseBlaster card.

during equal intervals. The data recorded by the counter card are processed by a data acquisition and analysis software (National Instruments LabVIEW) program. It combines the data with wavelength information provided by the wavemeter and information about the actual laser intensity provided by a power meter.

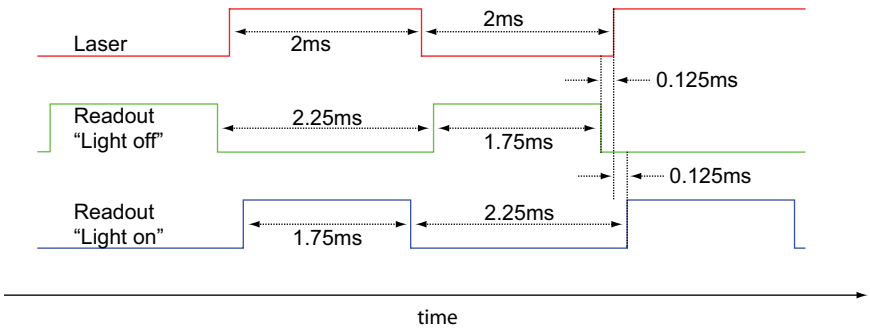

Fig. 3.8: Sequence of the PulseBlaster signals. The first channel (red) controls the frequency of the chopper. The second channel (green) gives a TTL pulse during light off intervals and the third channel (blue) during light on intervals.

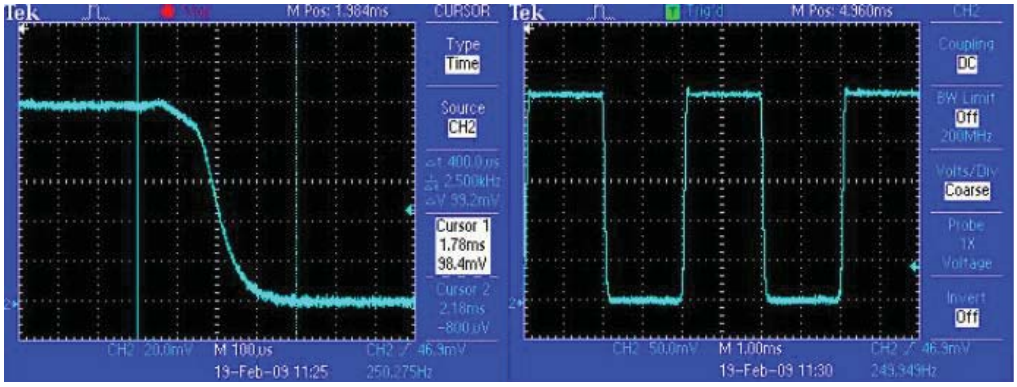

Fig. 3.9: Laser intensity signal produced by the chopper. On the left a falling edge is shown. The whole width of the picture is 1 ms and the range in which the rectangular signal is washed out is roughly 400 μs. On the right several pulses with a length of 2 ms are shown, which means that the chopper operates at a frequency of 250 Hz.

3.7 Course of a measurement

Before a measurement the source is heated up to evaporate enough cesium for proper operation. This is done with the filament and the cesium heater. Heating up the whole source ensures that not too much cesium condenses on the inner surfaces of the source. After a while this condensation would cause leakage currents, which would make a cleaning of the source necessary. When the source reaches its operating temperature ($\approx$ 480 K) the cathode and the rest of the source are set to the required electric potentials, depending on the desired beam energy. A first signal of the ion beam is then obtained on the first Faraday cup. In the next step the mass separation is adjusted and the desired isotope is selected from the mass spectrum. The signal is then optimized on the successive Faraday cups by varying the potentials of the einzel lens, the two quadrupole triplets, the bender and the spectrometer deflector. A first setting for the optimal potentials was obtained from ion optical simulations with SIMION.

Meanwhile the laser is started and roughly set to the desired wavelength by adjusting the crystal temperature and the etalon angle. Afterwards it takes some time until the OPO laser system reaches its stable operating temperature. As long as it is thermalizing the laser frequency drifts, causing an unstable operation with frequent mode jumps. When the drift decreases and the output power stabilizes the path of the laser beam through the spectroscopy arm of the apparatus is optimized using the CCD camera and a power meter which are positioned at a window behind the MCP (Fig. 3.2). The CCD camera is used to optimize on a sharp Gaussian beam profile and the power meter to optimize on maximum power. Then the frequency is finally adjusted to the desired value and an

automatic scan controlled, by the wavemeter, is started. Normally the wavemeter is set to follow a triangle function with an amplitude of some hundred MHz up to 1.5 GHz, depending on the purpose of the performed measurement. For a precision scan around a resonance an amplitude of roughly 200 MHz is chosen and the wavemeter is set to drive slow scans ($\approx$ 2 MHz/s) around the peak frequency. To obtain a good signal-to-noise ratio this is done several times and the data are later binned.

4. DIPOLE TRANSITION IN $^{192}OS^{-}$

As already mentioned in Chap. 2, the energy of the electric dipole (E1) transition was found to be 1.066316(19) eV in a previous experiment [12]. This corresponds to a frequency of 257.8341(46) THz. In this case the uncertainty of the transition of roughly 5 GHz was dominated by the bandwidth of the spectroscopy laser. Since the laser used in the UNIC experiment has a bandwidth below 5 MHz, a much better frequency resolution can be achieved.

In the setup used here, in contrast to the previous experiment, it is also possible to determine the cross section of the bound–bound E1 transition directly. Due to the use of the ionizer the two step process consisting of excitation and neutralization is reduced to the one step excitation (see Chap. 3.1), which allows to study the dipole transition separately.

4.1 Resonance frequency

In a collinear setup the resonance frequency is Doppler shifted (see Chap. 3.2). Since the ion and the laser beam are superimposed in a co-propagating geometry, the frequency is blue-shifted to higher frequencies. The rest frame resonance frequency can in principle be determined from a resonance frequency measurement at any given beam energy by use of Eq. (3.3). However, a possible beam energy offset can be determined (or ruled out) by carrying out measurements at different beam energies. The covered energy range reached from 2.5 keV to 6 keV in steps of 500 V. The determined resonance frequencies are shown in Tab. 4.1. A typical resonance is shown in Fig. 4.1, it was recorded at a beam energy of 5.5 keV. The blue curve was recorded with ionizer on and the red one with ionizer off. The difference between the two measurements clearly shows the dramatic enhancement of the detection efficiency due to the ionizer (roughly two orders of magnitude). The typical resonances have a width of $\Gamma_{\mathrm{res}} = 45$ MHz, which is dominated by the Doppler width of the ion beam. Except for a slight asymmetry the shape is compatible with a Gaussian profile. The asymmetry could be explained in the following way. The mass separator magnet is not only sensitive to the mass but also to the velocity of the particles. Therefore particles with the same mass but different velocities are deflected by different angles, resulting in a velocity gradient in the plane of the magnet. The slits after the mass separator allow only a small fraction of the ions to pass and cut not only ions with different masses, but also ions having the same mass but different velocities. In the interaction region the diameter of the ion beam is limited by the entrance diaphragm, which has an opening of 7.5 mm. The

Tab. 4.1: Blue-shifted resonance frequencies at ion beam energies from 2.5 to 6 keV. The uncertainties of the ion energy are due to fluctuations in the accelerating potential, whereas the frequency uncertainties result from the fits to the resonance curves.

Ion energy (eV)	**Transition frequency (MHz)**
2500(1)	257 874 317(35)
3000(1)	257 878 487(35)
3500(1)	257 882 216(35)
4000(1)	257 885 767(35)
4500(1)	257 889 033(35)
5000(1)	257 892 165(35)
5500(1)	257 895 168(35)
6000(1)	257 898 020(35)

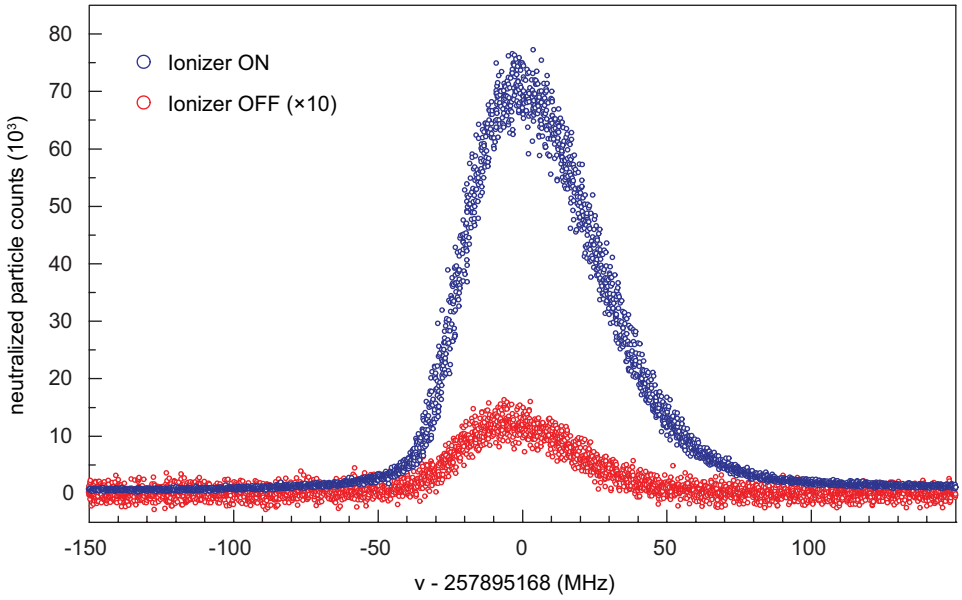

Fig. 4.1: Typical absorption/detachment resonances at a beam energy of 5.5 keV. The blue line was recorded with ionizer on and the red one with ionizer off. The efficiency gain due to the ionizer of about two orders of magnitude is clearly visible.

laser beam is collimated and has a smaller diameter of only about 1 mm. Hence only a part of the ion beam is illuminated by the laser, which also means that the laser only interacts with ions in a certain velocity range. This could result in the observed asymmetry of the velocity distribution of the ions and the corresponding asymmetry of the resonance. This hypothesis is supported by the fact that the asymmetry changed with different settings of the ion optical devices. This systematic effect is taken into account as an additional source of systematic uncertainty for the determined center frequency.

The recorded blue-shifted resonance frequencies were fitted with a function derived from Eq. (3.4):

$$\nu^{'} = \nu_0 \left(1 + \frac{1}{c} \sqrt{\frac{2e\left(U_{\mathrm{acc}} + \Delta U_{\mathrm{acc}}\right)}{m_{\mathrm{ion}}}} \right) \tag{4.1}$$

In this case the ion energy was replaced by $E_{\mathrm{ion}} = e(U_{\mathrm{acc}} + \Delta U_{\mathrm{acc}})$, where the additional factor ΔU_{acc} describes a possible offset of the acceleration voltage (result: $\Delta U_{\mathrm{acc}} = 0.4(5)\mathrm{V}$). The fit and its residuals are shown in Fig. 4.2. The resulting transition frequency of $\nu_0 = 257.831190(35)$ THz is consistent with the previous experimental value of 257.8341(46) THz, but the uncertainty was reduced by more than two orders of magnitude. The total uncertainty of the measurement of 35 MHz comprises an error due to the asymmetry of the resonances and an additional uncertainty due to the frequency measurement with the wavemeter, whose absolute accuracy is ±30 MHz.

4.2 Cross section

For the determination of the resonant cross section of the dipole transition in $^{192}\mathrm{Os}^-$ it is useful to consider the populations of the ground and the excited state and the numbers of already neutralized ions in the beam as a function of time of flight in the interaction region. The total number of particles and the laser power are assumed to be constant. As shown in [22], this leads to a system of three rate equations, one for each of the possible states of the ions:

$$\frac{dN_{\mathrm{g}}(t)}{dt} = -\ \sigma_0 \phi N_{\mathrm{g}}(t)\ +\ \left(\sigma_0 \phi + \tau_0^{-1}\right)\ N_{\mathrm{e}}(t), \tag{4.2a}$$

$$\frac{dN_{\mathrm{e}}(t)}{dt} = \sigma_0 \phi N_{\mathrm{g}}(t)\ -\ \left(\sigma_0 \phi + \tau_0^{-1} + \sigma_{\mathrm{d}} \phi\right)\ N_{\mathrm{e}}(t), \tag{4.2b}$$

$$\frac{dN_{\mathrm{d}}(t)}{dt} = \sigma_{\mathrm{d}} \phi N_{\mathrm{e}}(t), \tag{4.2c}$$

where $N_{\mathrm{g}}(t)$ and $N_{\mathrm{e}}(t)$ are the numbers of ions in the ground and the excited state, respectively and $N_{\mathrm{d}}(t)$ is the number of neutral atoms. σ_0 is the resonant cross section and σ_{d} the cross section for photo detachment. The laser power P_{laser} is connected to the

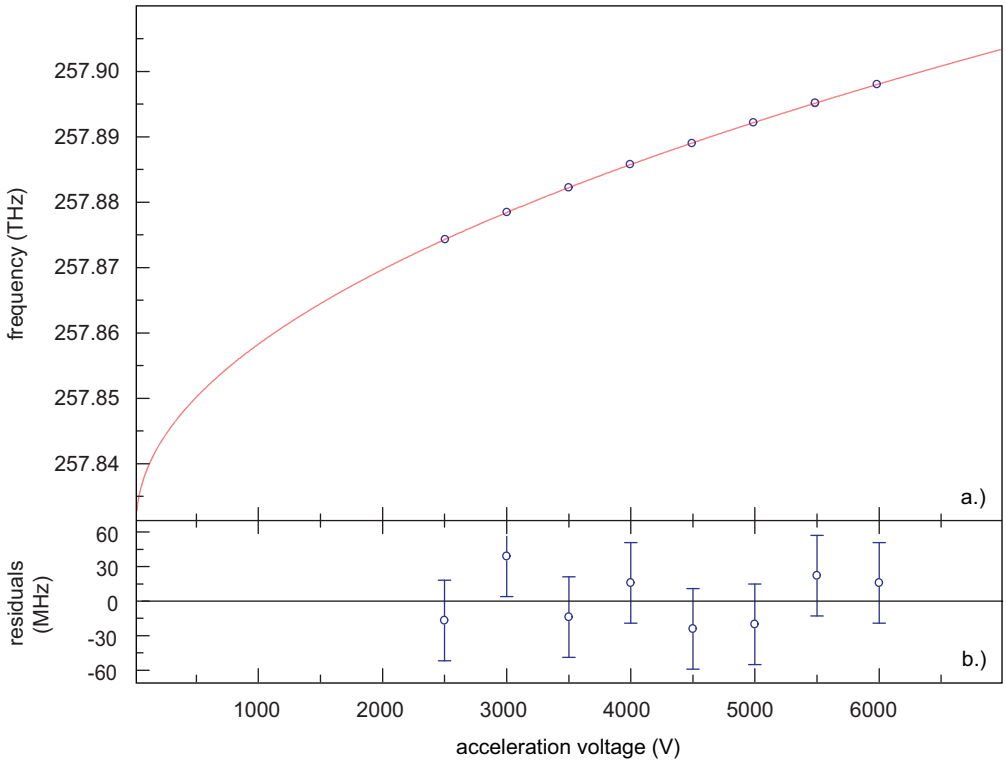

Fig. 4.2: a) Blue-shifted resonance frequencies as a function of the ion beam energy. The error bars are too small to be visible. The solid curve is the resulting fit for the Doppler shift. b) Residuals of the fit.

photon flux ϕ by the equation $P_{\text{laser}} = \phi h\nu$. The lifetime of the excited state with respect to decay into the ground state τ is related to σ_0 via

$$\tau_0 = c^2 / \left(4\pi^2 \sigma_0 \nu_0^2 \Gamma_{\text{res}}\right) . \tag{4.3}$$

In Eq. (4.3) Γ_{res} denotes the experimental width of the resonance, which was found to be 45 MHz. The additional detachment processes introduced in Chap. 3.1 were neglected in the rate equations, since it turned out that they do not affect the resulting cross section [22]. The other possible decay channels into the intermediate ($J = 7/2$ and $5/2$) states were also neglected because the partial lifetimes, which scale as ν^{-3}, are expected to be at least 8 times longer than τ.

The set of differential equations (4.2a)–(4.2c) can be solved analytically to obtain expressions for the number of ions in the excited state $N_{\text{e}}(t)$ and the number of detached atoms $N_{\text{d}}(t)$ as a function of the photon flux ϕ and the time of flight in the interaction region t. The photon flux was estimated to have a Gaussian profile in accordance with

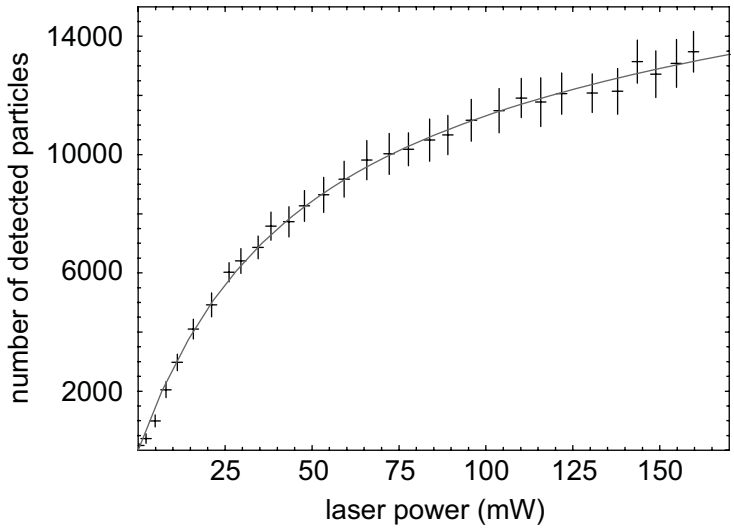

Fig. 4.3: Number of detected atoms as a function of laser intensity at the resonance frequency at a fixed ion beam energy of 2.5 keV. The solid curve is a fit to the data according to Eqs.(4.2a)–(4.2c), which yields the cross section σ_0 of the transition (Fig.5 of [22]).

observations made with the CCD beam profile camera installed behind the spectrometer. Excited ions reaching the ionizer are neutralized, therefore the number of neutralized ions behind the ionizer is $N_{\mathrm{neut}}(T, P_{\mathrm{laser}}, \sigma_0, \sigma_{\mathrm{d}}, N_0) = N_{\mathrm{e}}(T) + N_{\mathrm{d}}(T)$, where $T = L\sqrt{m/2eU_{\mathrm{acc}}}$ is the time of flight from the entrance diaphragm to the ionizer and $L = 520$ mm the distance between the two. N_{neut} is a function of the resonant and the non-resonant cross sections, the laser power and the total number of ions in the interaction region and can directly be measured on the MCP. It is very sensitive on the main parameter of interest σ_0.

The number of neutralized ions was measured for different ion beam energies from 2.5 to 5.5 keV as a function of the laser power, which was varied in a range from 0 to 160 mW using a polarizing beam splitter. Thereby the other laser beam characteristics were not affected. Figure 4.3 shows a typical measurement recorded at an ion beam energy of 2.5 keV. It is fitted with the function $N_{\mathrm{neut}}(P_{\mathrm{laser}})$ according to the rate equation model. The resonant cross section σ_0 was determined as a fit parameter. The final value $\sigma_0 = 2.5(7) \times 10^{-15}\ cm^2$ is the weighted mean of ten such measurements. In the uncertainty a possible ion beam divergence of 1.5° suggested by ion-optical simulations was taken into account. The cross section for laser detachment from the excited state σ_d could only be estimated from the fit as $\sigma_{\mathrm{d}} \approx 10^{-17}\ cm^2$. Using Eq. (4.3) the partial lifetime of the excited state for decay into the ground state by spontaneous emission was found to be $\tau_0 = 3(1)$ ms.

5. HYPERFINE STRUCTURE OF $^{187}OS^-$ AND $^{189}OS^-$

In atoms the gross structure of the energy levels is determined by the main quantum number n and the orbital angular momentum quantum number l. A more detailed investigation on the atomic structure reveals the *fine structure* splitting. In isotopes with odd mass numbers the fine structure levels are further split on a thousandfold smaller scale – the so called *hyperfine structure*. The hyperfine splitting contains information about the electron wavefunction of the system, which makes hyperfine structure measurements especially interesting for negative ions, where electron–electron correlations are of great importance and hard to calculate. In addition, the hyperfine structure can be used to determine unknown quantum numbers.

In the first part of this chapter the theoretical background of the fine and the hyperfine structure is presented. In the second part the measurements of the hyperfine structure of the bound–bound transition in $^{187}Os^-$ and $^{189}Os^-$ are discussed.

5.1 Theory

Fine Structure

In atoms the energy levels $E_{n,l}$ with orbital angular momentum $l \geq 1$ and spin $\boldsymbol{s}$ split up into two or more sublevels. This is the so called fine structure in atomic spectra. It is caused by a magnetic coupling of $\boldsymbol{l}$ and $\boldsymbol{s}$ to the total angular momentum $\boldsymbol{j}$:

$$\boldsymbol{j} = \boldsymbol{l} + \boldsymbol{s} \tag{5.1}$$

The absolute values of the angular momenta $\boldsymbol{l}$, $\boldsymbol{s}$ and $\boldsymbol{j}$ are defined as:

$$\begin{aligned} |\boldsymbol{l}| &= \sqrt{l\,(l+1)}\hbar \\ |\boldsymbol{s}| &= \sqrt{s\,(s+1)}\hbar \\ |\boldsymbol{j}| &= \sqrt{j\,(j+1)}\hbar, \end{aligned} \tag{5.2}$$

where j can take the values $|l - s| \leq j \leq l + s$.

The simplest atomic system is the hydrogen atom. In this special case the $E_{n,l}$ with $l \geq 1$ split up into 2 components. To calculate the energy shift due to the magnetic coupling one assumes an electron moving around the nucleus in circular orbits. Seen from a frame of reference in which the electron is stationary and the nucleus orbits it, the nucleus forms an

effective current loop, which creates a magnetic field. Using the well-known Biot-Savarts law one finds that the magnetic field created at the location of the electron is proportional to its orbital angular momentum:

$$\boldsymbol{B}_l = \frac{\mu_0 Ze}{4\pi r^3 m_\mathrm{e}} \boldsymbol{l}. \tag{5.3}$$

Due to its intrinsic angular momentum $\boldsymbol{s}$ the electron has a magnetic moment which interacts with the resulting magnetic field:

$$\boldsymbol{\mu}_s = -g_s \frac{e}{2m_\mathrm{e}} \boldsymbol{s}, \tag{5.4}$$

where g_s is the so called g-factor of the electron, $g_s \approx 2$. The interaction energy between the magnetic moment of the electron and the magnetic field is given by [23]:

$$V_{l,s} = -\boldsymbol{\mu}_s \cdot \boldsymbol{B}_l. \tag{5.5}$$

With Eqs. (5.3) and (5.4) and the fine structure constant $\alpha = \mu_0 Ze^2\hbar^2/(8\pi m_e^2 r^3)$ one finds:

$$V_{l,s} = \frac{a}{\hbar^2}\, \boldsymbol{s}\cdot\boldsymbol{l} = \frac{\alpha}{\hbar^2}\, |\boldsymbol{s}|\, |\boldsymbol{l}| \cos(\boldsymbol{s},\boldsymbol{l})\,. \tag{5.6}$$

In the fine structure constant α an additional factor 1/2 arises. This is the so-called Thomas-Factor, which is the result of the back transformation into the center-of-mass system of the atom.

Using the law of cosines applied to a triangle with the sides s_1, s_2, s_3 and the angle S_3 opposite with side s_3 and the definitions for $|\boldsymbol{s}|$, $|\boldsymbol{l}|$ and $|\boldsymbol{j}|$ [Eq. (5.2)] we obtain:

$$\begin{aligned} V_{l,s} &= \frac{a}{2\hbar^2}\left(|\boldsymbol{l}+\boldsymbol{s}|^2 - |\boldsymbol{l}|^2 - |\boldsymbol{s}|^2\right) \\ &= \frac{a}{2\hbar^2}\left(|\boldsymbol{j}|^2 - |\boldsymbol{l}|^2 - |\boldsymbol{s}|^2\right) \\ &= \frac{a}{2}\left[j\,(j+1) - l\,(l+1) - s\,(s+1)\right] = \Delta E_j. \end{aligned} \tag{5.7}$$

This is the formula for spin-orbit coupling or fine structure. It describes the splitting of the energy levels $E_{n,l}$ into the levels $E_{n,l,j}$:

$$E_{n,l,j} = E_{n,l} + \Delta E_j. \tag{5.8}$$

For a system with more than one electron a similar formula is used. But in this case one has to distinguish between two different limits, the LS-coupling and the jj-coupling, where the actual situation is always a mixture of both. Which limit is the better approximation depends on the energetic order of the different coupling energies.

LS coupling

If the coupling energy between the orbital magnetic moments of the single electrons [24]

$$V_{l_i,l_j} \propto \boldsymbol{l}_i \cdot \boldsymbol{l}_j \tag{5.9}$$

and the coupling energy between their spin magnetic moments

$$V_{s_i,s_j} \propto \boldsymbol{s}_i \cdot \boldsymbol{s}_j \tag{5.10}$$

is large compared to the coupling energy of the orbital magnetic moment and the spin magnetic moments of the single electrons

$$V_{l_i,s_i} \propto \boldsymbol{l}_i \cdot \boldsymbol{s}_i, \tag{5.11}$$

then all orbital angular momenta $\boldsymbol{l}_i$ combine to the total orbital angular momentum $\boldsymbol{L}$ and all spins $\boldsymbol{s}_i$ to the total spin $\boldsymbol{S}$:

$$\begin{aligned} \boldsymbol{L} &= \sum_i \boldsymbol{l}_i \\ \boldsymbol{S} &= \sum_i \boldsymbol{s}_i. \end{aligned} \tag{5.12}$$

The total angular momentum $\boldsymbol{J}$ of the electron shell is then:

$$\boldsymbol{J} = \boldsymbol{L} + \boldsymbol{S}, \quad \text{with} \quad |\boldsymbol{J}| = \sqrt{J\,(J+1)}\hbar \tag{5.13}$$

In this case the energy shift is quite similar compared to the one-electron-system:

$$\Delta E_J \propto \left[J\,(J+1) - L\,(L+1) - S\,(S+1)\right]. \tag{5.14}$$

The LS or *Russel-Saunders* coupling is prominent in light atoms with $Z < 30$.

jj coupling

In the case of jj coupling the coupling energy between the spin magnetic moments and the orbital magnetic moments of the single electrons [Eq. (5.11)] is larger then the spin–spin [Eq. (5.10)] and the orbit-orbit coupling [Eq. (5.9)]. In this case each orbital angular momentum $\boldsymbol{l}_j$ combines with the spin momentum $\boldsymbol{s}_j$ of the same electron. The resulting $\boldsymbol{j}_i$ combine then to the total angular momentum $\boldsymbol{J}$ of the electron shell:

$$\begin{aligned} \boldsymbol{j}_j &= \boldsymbol{l}_j + \boldsymbol{s}_j \\ \boldsymbol{J} &= \sum_i \boldsymbol{j}_i. \end{aligned} \tag{5.15}$$

The jj-coupling dominates over the LS-coupling in heavier atoms.

Hyperfine Structure

The hyperfine structure in atomic spectra denotes a further splitting of the fine structure levels, which due to the interaction between the nucleus and the electrons. It only occurs in atoms with a nuclear spin $I \neq 0$, which means in atoms with odd mass numbers. It consists of two main parts, the magnetic dipole (M1) and the electric quadrupole (E2) interactions. The separation of the spectral lines due to the hyperfine structure is roughly three orders of magnitude smaller than the one due to the fine structure, equal to the ratio between the magnetic moments of the nucleus and the electron. Thus a resolving power of $\approx 10^7$ is necessary to observe the hyperfine structure.

Magnetic-Dipole Interaction

To first order the nucleus is regarded as a point-like magnetic dipole which interacts with the magnetic field created by the moving electrons. Due to this interaction the total angular momentum of the electrons $\boldsymbol{J}$ and the nuclear spin $\boldsymbol{I}$ couple to the total angular momentum $\boldsymbol{F}$:

$$\begin{aligned} \boldsymbol{F} &= \boldsymbol{J} + \boldsymbol{I} \\ |\boldsymbol{F}| &= \sqrt{F\,(F+1)}\hbar \\ |\boldsymbol{I}| &= \sqrt{I\,(I+1)}\hbar. \end{aligned} \tag{5.16}$$

F can take the values $|J - I| \leq F \leq J + I$. Hence the number of possible F-states is:

$$\begin{aligned} n_F &= 2I + 1, \quad \text{for } I \leq J \\ n_F &= 2J + 1, \quad \text{for } J \leq I \end{aligned} \tag{5.17}$$

Due to the nuclear spin the nucleus has a magnetic moment:

$$\boldsymbol{\mu}_I = \frac{g_I \mu_\mathrm{N}}{\hbar} \boldsymbol{I}, \tag{5.18}$$

where g_I is the nuclear g-factor. μ_N is the nuclear magneton, $\mu_\mathrm{N} = e\hbar/2m_\mathrm{p} \approx \mu_\mathrm{B}/1836$, with the proton mass m_p and the Bohr magneton μ_B.

The moving electrons create a magnetic field $\boldsymbol{B_J}$ at the location of the nucleus. As in the case of the fine structure this magnetic field interacts with the magnetic moment of the nucleus [25]:

$$V_{IJ} = -\boldsymbol{\mu}_I \boldsymbol{B}_J. \tag{5.19}$$

Using $\boldsymbol{B}_J \propto \boldsymbol{J}$ [Eq. (5.18)] and the definition of $|\boldsymbol{I}|$ [Eq. (5.16)] one finds:

$$\begin{aligned} V_{IJ} &= -\mu_I B_J \cos\left(\boldsymbol{\mu}_I, \boldsymbol{B}_J\right) \\ &= g_I \mu_\mathrm{N} \sqrt{I\,(I+1)} B_J \cos\left(\boldsymbol{I}, \boldsymbol{J}\right). \end{aligned} \tag{5.20}$$

Due to the fact that $\boldsymbol{B}_J$ and $\boldsymbol{J}$ are anti-parallel [23], the sign is reversed in the second line of Eq. (5.20).

Using the law of cosines one finds:

$$\cos(\boldsymbol{I},\boldsymbol{J}) = \frac{F(F+1) - I(I+1) - J(J+1)}{2\sqrt{J(J+1)}\sqrt{I(I+1)}}. \tag{5.21}$$

With Eq. (5.21), Eq. (5.20) and the M1 constant A or Casimir factor

$$A = \frac{g_I \mu_N B_J}{\sqrt{J(J+1)}} \tag{5.22}$$

one finally finds for the energy shift due to the M1 interaction ΔE_F:

$$\Delta E_{M1} = \frac{A}{2} C,$$

where C is defined as:

$$C = [(F+1) - I(I+1) - J(J+1)]. \tag{5.23}$$

The energy gap between two hyperfine structure levels with F and $F' = F+1$ is given by the interval rule:

$$\Delta E_{M1}(F) - \Delta E_{M1}(F+1) = A(F+1). \tag{5.24}$$

Therefore the intervals in a hyperfine structure multiplet observe a ratio $F : (F-1) : (F-2)$, etc. This is the origin of the historical name of the magnetic-dipole constant A, which is interval factor.

Electric-Quadrupole Interaction

In 1935 Schüler and Schmidt experimentally studied the hyperfine structure of ^{151}Eu and ^{153}Eu and found small deviations from the pattern one would expect due to the M1 interaction [26]. They assumed that the variations could be due to a non-spherical charge distribution in the nucleus. In the same year Casimir interpreted this behavior as an electric-quadrupole moment of the nucleus interacting with the electric field of the electron shell [27]. Since nuclei with nuclear spin $I = 0$ and $I = 1/2$ have spherically symmetric charge distributions [25], the electric-quadrupole moment is only found in nuclei with $I \geq 1$.

A simplified deviation of the electric-quadrupole interaction is obtained by considering the energy of a charge distribution $\rho(\boldsymbol{r})$ in an external potential $\phi(\boldsymbol{r})$:

$$E = \int dV \rho(\boldsymbol{r}) \phi(\boldsymbol{r}). \tag{5.25}$$

Taking into account that the external potential varies only little near the origin, one can develop it in a Taylor series:

$$\phi(\boldsymbol{r}) = \phi(0) + (\boldsymbol{r}\cdot\nabla)\,\phi(\boldsymbol{r}')\,|_{r'=0} + 1/2\,(\boldsymbol{r}\cdot\nabla)^2\,\phi(\boldsymbol{r}')\,|_{r'=0} + ... \tag{5.26}$$

Plugging Eq. (5.26) into Eq. (5.25) one finds:

$$E = \int dV \rho(\boldsymbol{r})\,\phi(0) + \int dV \rho(\boldsymbol{r})\,\boldsymbol{r}\nabla\phi(\boldsymbol{r}') + \frac{1}{2}\sum_{i,j}\int dV \rho(\boldsymbol{r})\,x_i x_j \frac{\partial\phi(\boldsymbol{r}')}{\partial x_i \partial x_j} + ... \tag{5.27}$$

The first term of Eq. (5.27) is the E0 interaction , the second one the E1 interaction and the third one the E2 interaction. The E0 term describes a point-like nucleus, which leads to the main energetic order in an atom. A permanent electric-dipole moment has never been found to in any nucleus [28, 29]. Its existence would violate time reversal symmetry (T), which would also imply violation of the CPT theorem.

The remaining E2 interaction contains the quadrupole moment, which is a 2nd order tensor. Assuming that the nucleus is axially symmetric, the non-diagonal entries of the quadrupole tensor vanish and only the diagonal entries remain:

$$E_{\mathrm{E2}} = \frac{1}{2}\sum_i \int dV \rho(\boldsymbol{r})\,{x_i}^2 \frac{\partial^2\phi(\boldsymbol{r}')}{\partial x_i^2}. \tag{5.28}$$

Furthermore the potential used in Eq. (5.26) satisfies the Laplace equation:

$$\Delta\phi = 0. \tag{5.29}$$

Using the coordinate system (x, y, z) for the potential and assuming an axial symmetry with respect to the z-axis, defined by the orientation of the total angular momentum $\boldsymbol{J}$, the following relation is fulfilled:

$$\frac{\partial^2\phi}{\partial z^2} = -2\frac{\partial^2\phi}{\partial x^2} = -2\frac{\partial^2\phi}{\partial y^2}. \tag{5.30}$$

It simplifies Eq. (5.28) in the following way:

$$E_{\mathrm{E2}} = \frac{1}{4}\frac{\partial^2\phi}{\partial z^2}\int dV \left(3z^2 - r^2\right)\rho(\boldsymbol{r}). \tag{5.31}$$

The axis of symmetry of the nucleus, given by the nuclear spin $\boldsymbol{I}$, is tilted by an angle θ against $\boldsymbol{J}$. Therefore the coordinate system (ξ, η, ζ) of the nucleus (with axis of symmetry

ζ) has to be shifted into the coordinate system of the electric potential and Eq. (5.31) is transformed to:

$$\begin{aligned} E_{\mathrm{E2}} &= \frac{1}{4}\frac{\partial^2\phi}{\partial z^2}\int dV\left(3z^2-r^2\right)\rho\left(\boldsymbol{r}\right)\left(3/2\cos^2\theta-1/2\right) \\ &= \frac{1}{4}\,e\,Q\,\frac{\partial^2\phi}{\partial z^2}\left(3/2\cos^2\theta-1/2\right), \quad \text{with} \quad e\,Q=\int dV\left(3z^2-r^2\right)\rho\left(\boldsymbol{r}\right), \end{aligned} \tag{5.32}$$

where Q is the quadrupole moment of the nucleus. Since ζ and z are parallel to $\boldsymbol{I}$ and $\boldsymbol{J}$, θ is also the angle between the two angular momenta. Thus $\cos^2\theta$ can be expressed in terms of $\boldsymbol{I}$ and $\boldsymbol{J}$ using the law of cosines and one finally finds for the quadrupole interaction:

$$\begin{aligned} E_{\mathrm{E2}} &= \frac{B}{2}\frac{\frac{3}{4}\left(\boldsymbol{F}^2-\boldsymbol{I}^2-\boldsymbol{J}^2\right)^2-\boldsymbol{I}^2\boldsymbol{J}^2}{4\boldsymbol{I}^2\boldsymbol{J}^2} \\ &= \frac{B}{2}\frac{\frac{3}{4}\,C^2-I\left(I+1\right)J\left(J+1\right)}{4I\left(I+1\right)J\left(J+1\right)}, \end{aligned} \tag{5.33}$$

where

$$B=\,e\,Q\,\frac{\partial^2\phi}{\partial z^2} \tag{5.34}$$

is the E2 constant and C is defined by Eq. (5.23).

A rigorous quantum mechanical calculation yields a slightly different result, but in the limit of large quantum numbers it agrees quite well [28]:

$$\Delta E_{\mathrm{E2}}=\frac{B}{2}\;D$$

with

$$D=\frac{\frac{3}{4}\,C\left(C+1\right)-I\left(I+1\right)J\left(J+1\right)}{I\left(2I-1\right)J\left(2J-1\right)}. \tag{5.35}$$

Equation (5.35) is the standard formula for the energy shift due to the E2 interaction.

Energy Shift due to the Hyperfine Interaction

Neglecting higher orders the total energy shift due to the hyperfine interaction is composed of the M1 and the E2 interaction. The formula which describes the entire effect is the Casimir formula:

$$\begin{aligned} \Delta E_F &= \Delta E_{\mathrm{M1}}+\Delta E_{\mathrm{E2}} \\ &= \frac{A}{2}\,C+\frac{B}{2}\,D \end{aligned} \tag{5.36}$$

The hyperfine structure constants A and B are normally roughly of the same order, which results in a main structure due to the M1 interaction and smaller corrections due to the

E2 interaction, because $A \gg B$. The total energy of a state in an atom with non vanishing a nuclear spin is made up of the energy due to simple Coulomb interaction and shifts due to the fine and the hyperfine coupling:

$$E_{n,L,J,F} = E_{n,L} + \Delta E_J + \Delta E_F. \tag{5.37}$$

5.2 Measurements and results

For the analysis of the hyperfine structure of $^{187}Os^-$ and $^{189}Os^-$ their optical spectra around 1163 nm were recorded. In the following the study on $^{187}Os^-$ will be explained in detail and the developed procedure will later be used for a brief discussion of $^{189}Os^-$.

Figure 5.1 shows the hyperfine structure of $^{187}Os^-$. The spectrum contains four resonances in total, two strong central ones and two weaker lateral ones. The stronger resonances are due to transitions between states with $\Delta F = 0$. Due to the fact that these transitions are about one order of magnitude stronger than transitions with $\Delta F \pm 1$ one refers to them as "principal lines", while the weaker ones are called "satellites" [30].

For the calculation of the hyperfine structure constants A and B on the basis of the measured spectra, the quantum numbers of the $^4F_{9/2}$ ground and the $^6D_{J_{e1}}$ excited state have to be known. Therefore one must first determine the total angular momentum J_{e1} of the excited state. Due to the hyperfine interaction the $^4F_{9/2}$ ground and the $^6D_{J_{e1}}$ excited state of the E1 transition split up into $2I+1$ sublevels [Eq. (5.17)]. This means for $^{187}Os^-$ ($I = 1/2$) that both levels split up into two components and for $^{189}Os^-$ ($I = 3/2$) into four components. E1 transitions are only possible between hyperfine structure levels which fulfill the standard selection rules:

$$\Delta J = J_e - J_g = 0, \pm 1, \tag{5.38a}$$

$$\Delta F = F_e - F_g = 0, \pm 1. \tag{5.38b}$$

Since the $^4F_{9/2}$ ground state has a total angular momentum of $J = 9/2$, the $^6D_{J_{e1}}$ excited state could have a total angular momentum of $J_{e1} = 7/2,\ 9/2$ or $11/2$. The number of allowed transitions between the hyperfine levels is restricted by Eq. (5.38b). Assuming that $J_{e1} = 7/2$ or $11/2$ there would be three allowed transitions for $^{187}Os^-$ and nine for $^{189}Os^-$. In case of $J_{e1} = 9/2$ it would be four for $^{187}Os^-$ and ten for $^{189}Os^-$. Hence it can already be deduced from Fig. 5.1 that the total angular momentum of the excited state $J_{e1} = 9/2$.

To make sure that all four resonances belong to the spectrum of $^{187}Os^-$ and are not resonances of other isotopes in the ion beam, several spectra were recorded at different magnetic fields of the mass separator and compared. A resonance which belongs to a neighboring isotope would become stronger when the mass separator setting approaches a better setting for this particle, while the $^{187}Os^-$ resonances would become weaker. Since all resonances became weaker by tuning away from the ideal mass separator setting, all of them are assumed to belong to the spectrum of $^{187}Os^-$.

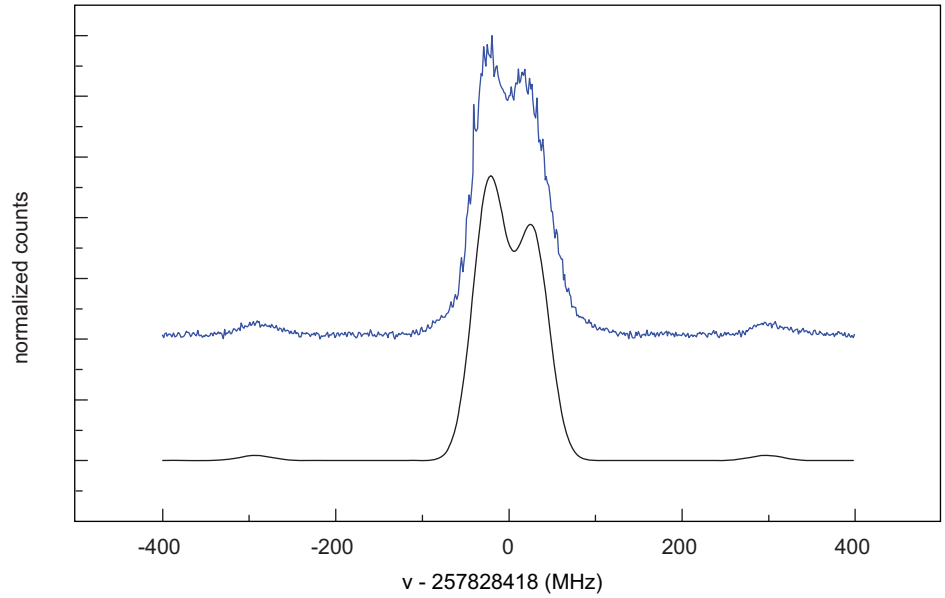

Fig. 5.1: Hyperfine structure of $^{187}Os^{-}$. The two strong resonances are transitions with $F = F^{'}$ and the two weak ones with $F = F^{'} \pm 1$. Below is a spectrum consisting of a superposition of four Gaussian curves showing the theoretical relative intensities.

Tab. 5.1: Left: experimental values of the rest frame frequencies of the different peaks in the spectrum of $^{187}Os^{-}$ and their relative intensities in the order of their strengths. Right: theoretical relative intensities of the transitions between the $^{4}F_{9/2}$ ground and the $^{6}D_{9/2}$ excited state hyperfine structure multiplets.

experimental		**theoretical**	
frequency (MHz)	**rel. intensity (%)**	$F \rightarrow F^{'}$	**rel. intensity (%)**
257 828 395(35)	100	$5 \rightarrow 5$	100.0
257 828 445(35)	88	$4 \rightarrow 4$	81.6
257 828 125(35)	4	$5 \rightarrow 4$	1.9
257 828 715(35)		$4 \rightarrow 5$	

The resonances were fitted with a superposition of four Gaussian curves, leaving the center positions and intensities as free parameters. The peak width was kept fixed at 45 MHz, consistent with the width of the resonance of $^{192}Os^{-}$. As already discussed in Chap. 4.1, the peaks are slightly asymmetric and the final uncertainty of the determined frequencies is 35 MHz. On the basis of the measured data the rest frame frequencies were calculated, using the transition in $^{192}Os^{-}$ as a reference and thereby deducing the blue-shift of the determined frequencies. The deduced values including the relative intensities of the different peaks are summarized in Tab. 5.1.

For the calculation of the hyperfine structure constants of the ground and the excited states Eq. (5.37) is used which describes the energy $E_{n,L,J,F}$ of the hyperfine structure levels. The observed resonances are transitions between hyperfine structure sublevels of the $^4F_{9/2}$ ground and the $^6D_{9/2}$ excited states. Hence their energy is the difference of the energies of the involved sublevels:

$$\begin{aligned} h\nu_{FF'} &= E^{e}_{n',L',J',F'} - E^{g}_{n,L,J,F} \\ &= E^{e}_{n',L'} + \Delta E^{e}_{J'} + \Delta E^{e}_{F'} - \left(E^{g}_{n,L} + \Delta E^{g}_{J} + \Delta E^{g}_{F}\right) \\ &= \underbrace{E^{e}_{n',L'} + \Delta E^{e}_{J'} - E^{g}_{n,L} - \Delta E^{g}_{J}}_{h\nu_0} + \Delta E^{e}_{F'} E - \Delta E^{g}_{F} \\ &= h\nu_0 + \Delta E^{e}_{F'} - \Delta E^{g}_{F}, \end{aligned} \tag{5.39}$$

where the E^{e} belong to the excited state and the E^{g} to the ground state of the transition. The energy shifts $\Delta E^{e}_{F'}$ and ΔE^{g}_{F} are given by Eq. (5.36) and describe the splitting due to the hyperfine interaction. The frequency ν_0 is the resonance frequency between the degenerate fine structure energy levels, or the center-of-gravity frequency of the hyperfine spectrum. With Eq. (5.36) one finds for the frequencies of the transitions $F \rightarrow F'$ between the two multiplets:

$$\nu_{FF'} = \nu_0 + \frac{1}{2h}\left(A^{e}C^{e} + B^{e}D^{e} - A^{g}C^{g} - B^{g}D^{g}\right), \tag{5.40}$$

where the parameter C is given by Eq. (5.23) and D by Eq. (5.35). This yields a system of equations with one equation for each of the possible transitions. To solve the system it is necessary to assign the measured transition frequencies to the corresponding equations. This is done based on the characteristic intensity of each transition. The measured intensities were compared with calculated values gained from the Eqs. (A.2a) – (A.2c). The resulting values are given in Tab. 5.1. In this context the problem arises, that transitions $F_1 \rightarrow F_2$ have the same intensity as transitions $F_2 \rightarrow F_1$ (see Tab. 5.1). Hence only the transitions with $F = F'$ can definitely be assigned to one of the frequencies. For the rest there are two different possibilities which leads to two systems of equations and consequently also to two different sets of hyperfine structure constants.

In Eq. (5.40) the hyperfine structure constants A and B lead to shifts away from the center of gravity frequency ν_0 and therefore depend only on the relative position of the

Tab. 5.2: The two sets of calculated M1 and E2 constants and the center-of-gravity frequency ν_0 for $^{187}Os^-$ and $^{189}Os^-$.

$^{187}Os^-$	**Set 1**		**Set 2**		
state	A	B	A	B	ν_0 (MHz)
$^4F_{9/2}$	64(2)	-	-54(2)	-	257828418(35)
$^6D_{9/2}$	54(2)	-	-64(2)	-	

$^{189}Os^-$	**Set 1**		**Set 2**		
state	A	B	A	B	ν_0 (MHz)
$^4F_{9/2}$	216(2)	396(4)	-184(2)	-479(4)	257829617(35)
$^6D_{9/2}$	184(2)	479(4)	-216(2)	-396(4)	

measured frequencies. In contrast to the absolute uncertainties of 35 MHz given in Tab. 5.1, the relative uncertainty is much smaller, especially in case of the hyperfine structure, where the single resonance frequencies are close to each other. The systematic uncertainty resulting from the wavemeter drift was estimated to be 3 MHz. In the case of $^{187}Os^-$ the nuclear spin is $I = 1/2$ and the nucleus has no quadrupole moment (Sec.5.1). Therefore the hyperfine splitting is only due to the M1 interaction, and the two systems of equations based on Eq. (5.40) have three variables. The M1 constants of the ground and the excited states, A^g and A^e and the center of gravity frequency ν_0. The values resulting from solving the two systems of equations are given in Tab. 5.2.

For $^{189}Os^-$ the same procedure as for $^{187}Os^-$ was used for the evaluation. Ten peaks are shown in the hyperfine structure spectrum (Fig. 5.3), which confirms that the total angular momentum of the excited state is $J_{e1} = 9/2$. This time the spectrum consists of four strong resonances in the center and three weaker ones on each side. Near the edge of the left of the two central strong peaks an eleventh resonance is visible. By the method of recording spectra while scanning the mass separator field, as described above, it was ruled out that this extra resonance belongs to the spectrum of another isotope. The rest frame frequencies and the intensities of the resonances are given in Tab. 5.3. Like for $^{187}Os^-$, among the weak resonances are always two with the same intensity, which leads to two systems of equations resulting in two sets of variables (Tab. 5.2).

Using only experimental information, some freedom remains in the assignment of the hyperfine structure constants (Sets 1 and 2 in Tab. 5.2). Fortunaltely some calculations exist on the hyperfine splitting of the $^4F^e_{9/2}$ ground state of $^{189}Os^-$ [13]. The M1 constant A and the E2 constant B were calculated using Dirac Fock (DF) and Relativistic Configuration Interaction (RCI) methods. The theoretical values are given in Tab. 5.4. A characteristic feature of the theoretical values is that they are all positive. This is only the

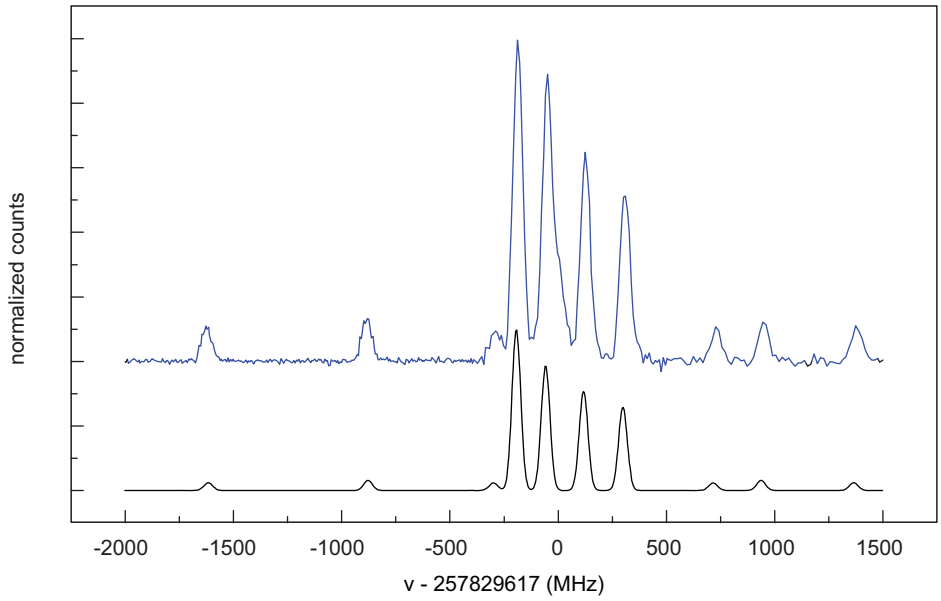

Fig. 5.2: Hyperfine structure of $^{189}Os^{-}$. The four strong resonances are transitions with $F = F^{'}$ and the six weak ones with $F = F^{'} \pm 1$. Below is a spectrum consisting of a superposition of ten Gaussian curves showing the theoretical relative intensities.

Tab. 5.3: Left: experimental values of the rest frame frequencies of the different peaks in the spectrum of $^{189}Os^{-}$ and their relative intensities in the order of their strengths. Right: theoretical relative intensities of the transitions between the $^{4}F_{9/2}$ ground and the $^{6}D_{9/2}$ excited state hyperfine structure multiplets.

experimental		**theoretical**	
frequency (MHz)	**rel. intensity (%)**	$F \rightarrow F^{'}$	**rel. intensity (%)**
257 829 423(35)	100	$6 \rightarrow 6$	100.0
257 829 557(35)	88	$5 \rightarrow 5$	77.7
257 829 733(35)	67	$4 \rightarrow 4$	61.6
257 829 915(35)	53	$3 \rightarrow 3$	51.7
257 828 740(35)	13	$5 \rightarrow 4$	6.3
257 830 554(35)		$4 \rightarrow 5$	
257 828 001(35)	11	$6 \rightarrow 5$	4.8
257 830 983(35)		$5 \rightarrow 6$	
257 829 318(35)	10	$4 \rightarrow 3$	4.7
257 830 334(35)		$3 \rightarrow 4$	

Tab. 5.4: Resulting experimental values for the M1 constant A and the E2 constant B for the $^4F_{9/2}$ and the $^6D_{9/2}$ state in $^{187}Os^-$ and $^{189}Os^-$. The theoretical values are taken from Ref. [13].

		experimental		**theoretical**			
isotope	**state**	A	B	A_{DF}	B_{DF}	A_{RCI}	B_{RCI}
$^{187}Os^-$	$^4F_{9/2}$	64(2)	-	-	-	-	-
	$^6D_{9/2}$	54(2)	-	-	-	-	-
$^{189}Os^-$	$^4F_{9/2}$	216(2)	396(4)	214	420	386	381
	$^6D_{9/2}$	184(2)	479(4)	-	-	-	-

case for the experimental values belonging to Set 1 in Tab. 5.2. The theoretical value for the M1 constant derived from the RCI method $A_{RCI} = 214$ MHz reproduces the experimental value $A = 216(2)$ MHz of Set 1 quite well. The same is the case for both theoretical values for the E2 constant B.

Altogether this is a strong hint that Set 1 is the correct one for $^{189}Os^-$. Using the definition of A from Eq. (5.22) it is possible to identify the correct set of variables for $^{187}Os^-$ on the basis of the knowledge about the variables of $^{189}Os^-$. For this purpose one has to divide Eq. (5.22) for $^{189}Os^-$ by Eq. (5.22) for $^{187}Os^-$:

$$\frac{A_{^{189}Os^-}}{A_{^{187}Os^-}} = \frac{\mu_{^{189}Os}\, I_{^{187}Os}}{\mu_{^{187}Os}\, I_{^{189}Os}}, \tag{5.41}$$

where μ is the magnetic moment of the nucleus and $\boldsymbol{I}$ the nuclear spin. The ratio of the magnetic moments of ^{189}Os and ^{187}Os is $\mu_{^{189}Os}/\mu_{^{187}Os} = 10.2075(1)$ [31]. With the ground state splitting constant of $^{189}Os^-$, $A^g_{^{189}Os} = 216(2)$ MHz, Eq. (5.41) gives $A^g_{^{187}Os} = 63.5(6)$ MHz. This result leads to the conclusion that also for $^{187}Os^-$ Set 1 is correct. The final experimental values derived from the hyperfine structure measurements are given in Tab. 5.4, and the corresponding energy level diagrams of the hyperfine splitting of the $^6D_{9/2}$ and the $^4F_{9/2}$ states in $^{189}Os^-$ and $^{187}Os^-$ are given in the appendix (Fig. A.1).

6. ISOTOPE SHIFT

In different isotopes of the same element the frequencies of the spectral lines are slightly different. This phenomenon is called *isotope shift*. Adding an additional neutron to a nucleus makes it first heavier and second changes its charge distribution and radius. Both affects the energy levels of the atom: due to the heavier nucleus the center of gravity of the whole system, namely nucleus and electron shells, is shifted closer to the center of the nucleus, which impacts the electron motion. This is the so called *mass effect* (or mass shift). Since the effect of an additional neutron on the center of mass decreases with higher mass numbers the mass effect is more prominent in light elements. The change in the charge distribution and the radius of the nucleus affects the potential experienced by the electrons within the nucleus. Due to the huge overlap of their wavefunctions with the nucleus, especially s and p electrons are affected. This is the so called *field* or *volume effect* (or field shift). Elements with high mass numbers have larger nuclei and potentially more overlap of the electron wavefunctions with the nucleus. Therefore the field effect is dominating in heavy atoms over the mass effect. The isotope shift of a spectral line observed between two isotopes with mass numbers A and A' is usually given as the sum of the mass (MS) and the field shift (FS) [32]:

$$\delta\nu^{A,A'} = \delta\nu_{\mathrm{MS}}^{A,A'} + \delta\nu_{\mathrm{FS}}^{A,A'} \tag{6.1}$$

6.1 Theory

Mass shift

To describe the MS we start with the kinetic energy operator in the Schrödinger equation [33]:

$$T = \frac{\boldsymbol{p}_{\mathrm{n}}^2}{2m_{\mathrm{n}}} + \sum_i \frac{\boldsymbol{p}_i^2}{2m_{\mathrm{e}}}, \tag{6.2}$$

where p_{n} and m_{n} are the momentum and the mass of the nucleus and p_i and $\mathrm{m_e}$ the momentum and the mass of the i-th electron.

In a stationary atom it follows from momentum conservation that:

$$\boldsymbol{p}_{\mathrm{n}} = -\sum_i \boldsymbol{p}_i, \tag{6.3}$$

therefore Eq. (6.2) can be rewritten as:

$$\begin{aligned} T &= \frac{\left(\sum_i \boldsymbol{p}_i\right)^2}{2m_\mathrm{n}} + \sum_i \frac{\boldsymbol{p}_i^2}{2m_\mathrm{e}} \\ &= \frac{\sum_i \boldsymbol{p}_i^2}{2m_\mathrm{n}} + \frac{1}{m_\mathrm{n}} \sum_{i>j} \boldsymbol{p}_i \boldsymbol{p}_j + \sum_i \frac{\boldsymbol{p}_i^2}{2m_\mathrm{e}}. \end{aligned} \tag{6.4}$$

Introducing the reduced mass $\mu = m_\mathrm{e} m_\mathrm{n} / \left(m_\mathrm{e} + m_\mathrm{n}\right)$, the first and the last term in Eq. (6.4) can be combined:

$$T = \frac{\sum_i \boldsymbol{p}_i^2}{2\mu} + \frac{1}{m_\mathrm{n}} \sum_{i>j} \boldsymbol{p}_i \boldsymbol{p}_j. \tag{6.5}$$

The first term in Eq. (6.5) is the so called *normal mass shift* (NMS) and the second one the *specific mass shift* (SMS). The NMS is simply due to the reduced-mass correction and the SMS is a correction due to correlations in the electron motion influencing the recoil energy of the nucleus [34]. In a first step the SMS term will be ignored and investigated separately later.

Denoting E_∞ the energy of a transition in a fictitious isotope with infinite nuclear mass and E_{m_n} the energy of the same transition in an isotope with nuclear mass m_n, E_{m_n} can be written as [33]:

$$E_{m_\mathrm{n}} = E_\infty \frac{m_\mathrm{n}}{m_\mathrm{n} + m_\mathrm{e}} = E_\infty \frac{\mu}{m_\mathrm{e}}, \tag{6.6}$$

which is derived from the solution of the Schrödinger equation for the hydrogen atom. The normal mass shift of the isotope with mass m_n with respect to the fictitious isotope with infinite mass is then:

$$\delta E_\mathrm{NMS}^{m_\mathrm{n},\infty} = E\left(m_\mathrm{n}\right) - E\left(\infty\right) = -E\left(\infty\right) \frac{m_\mathrm{e}}{m_\mathrm{n} + m_\mathrm{e}}. \tag{6.7}$$

Using the approximation $m_\mathrm{n} m_\mathrm{n}' \gg m_\mathrm{e}^2 - m_\mathrm{n} m_\mathrm{e} - m_\mathrm{n}' m_\mathrm{e}$, one finds for the NMS of the transition between two isotopes with nuclear masses m_n and m_n':

$$\delta E_\mathrm{NMS}^{m_\mathrm{n},m_\mathrm{n}'} \approx -E\left(\infty\right) \frac{m_\mathrm{e}\left(m_\mathrm{n} - m_\mathrm{n}'\right)}{m_\mathrm{n} m_\mathrm{n}'}. \tag{6.8}$$

Finally the frequency shift is:

$$\delta \nu_\mathrm{NMS}^{m_\mathrm{n},m_\mathrm{n}'} \approx -\frac{m_\mathrm{e}\left(m_\mathrm{n} - m_\mathrm{n}'\right)}{m_\mathrm{n} m_\mathrm{n}'} \nu_\infty = \nu_\infty \frac{m_\mathrm{e}}{m_\mathrm{u}} \frac{A - A'}{A A'}, \tag{6.9}$$

where A and A' denote the atomic masses of the two isotopes, m_u the atomic mass unit and ν_∞ the transition frequency in the fictitious isotope with infinite mass.

As said before the second term in Eq. (6.5) is due to the specific mass shift. It contains the dot product of the electron momenta and can also be written in operator-form:

$$\frac{1}{m_\mathrm{n}} \sum_{i>j} \boldsymbol{p}_i \boldsymbol{p}_j = \left(-\hbar^2/m_\mathrm{n}\right) \sum_{i>j} \nabla_i \nabla_j. \tag{6.10}$$

As an approximation the operator can be treated by perturbation theory. In first order this leads to an energy shift with respect to the reference level E_∞ [33]:

$$\delta E_\mathrm{SMS}^{m_\mathrm{n},\infty} = -\frac{\hbar^2}{m_\mathrm{n}} \sum_{i>j} \int \Psi^* \nabla_i \nabla_j \Psi dV, \tag{6.11}$$

where Ψ is the many-electron wavefunction and the range of integration is the volume of the atom.

Comparing again the shift of two isotopes with nuclear masses m_n and m'_n one finds:

$$\delta E_\mathrm{SMS}^{m_\mathrm{n},m'_\mathrm{n}} = -\frac{(m_\mathrm{n} - m'_\mathrm{n})}{m_\mathrm{n} m'_\mathrm{n}} \hbar^2 \sum_{i>j} \int \Psi^* \nabla_i \nabla_j \Psi dV \propto \frac{A - A'}{AA'}. \tag{6.12}$$

Therefore the SMS can be written as:

$$\Delta\nu_\mathrm{SMS}^{A,A'} = M_\mathrm{SMS} \frac{A - A'}{AA'}, \tag{6.13}$$

with M_SMS being the SMS coefficient. The NMS can be written in the same way with the NMS coefficient $M_\mathrm{NMS} = \nu_\infty m_\mathrm{e}/m_\mathrm{u}$

$$\Delta\nu_\mathrm{NMS}^{A,A'} = M_\mathrm{NMS} \frac{A - A'}{AA'}, \tag{6.14}$$

and finally the total mass shift is:

$$\delta\nu_\mathrm{MS}^{A,A'} = M_\mathrm{MS} \frac{A - A'}{AA'}\ , \quad \text{with} \quad M_\mathrm{MS} = M_\mathrm{NMS} + M_\mathrm{SMS}. \tag{6.15}$$

Field shift

The field shift originates from changes in the nuclear charge distribution and size between different isotopes. Therefore one may approximate it by comparing atoms with a fictitious, point-like nucleus and an extended nucleus. To first order the contribution to the energy shift of an electron term is the expectation value of the electrostatic potential energy difference $V(r) - V_0(r)$, where $V(r)$ is the potential energy for an extended nucleus and $V_0(r)$ the one for a point nucleus. Thus the energy shift is [33]:

$$\begin{aligned} \Delta E_\mathrm{FS} &= \int_0^\infty \Psi^* \left(V(r) - V_0(r)\right) \Psi 4\pi r^2 dr \\ &\approx \int_0^{r_0} \Psi^* \Delta V(r) \Psi 4\pi r^2 dr, \end{aligned} \tag{6.16}$$

where Ψ is the electron wavefunction and r_0 the radius of the nucleus. In this equation the range of integration was restricted to $0 \leq r \leq r_0$, since $V(r) = V_0(r)$ for $r \geq r_0$ by Gauss's theorem.

The difference of the energy shift in an isotope with mass number A and a second isotope with mass number A' is:

$$\delta E_{\mathrm{FS}}^{A,A'} = \Delta E_{\mathrm{FS}}^{A} - \Delta E_{\mathrm{FS}}^{A'}. \tag{6.17}$$

By solving the integral and factor the result, Eq. (6.17) can be written as [28]:

$$\begin{aligned} \delta E_{\mathrm{FS}}^{A,A'} &= \frac{\pi a_0^3}{Z} \Delta \left|\Psi(0)\right|^2 f(Z) \lambda(A, A') \\ &= F \lambda(A, A'), \end{aligned} \tag{6.18}$$

where a_0 is the Bohr radius and $f(Z)$ is a function that describes relativistic corrections, which increases with Z. The factor $\lambda(A, A')$ describes the nucleus and can be developed in a series of the change in mean square nuclear radii $\delta \left\langle r^2 \right\rangle^{A,A'}$ between the two isotopes with mass numbers A and A' [34]:

$$\lambda(A, A') = \delta \left\langle r^2 \right\rangle^{A,A'} + \frac{C_2}{C_1} \delta \left\langle r^4 \right\rangle^{A,A'} + \frac{C_3}{C_1} \delta \left\langle r^6 \right\rangle^{A,A'} + ... \tag{6.19}$$

The ratios C_i/C_1 were for example calculated by Seltzer [35].

To a good approximation the higher orders of Eq. (6.19) can be neglected [34] and therefore

$$\lambda(A, A') = \delta \left\langle r^2 \right\rangle^{A,A'} \tag{6.20}$$

will be used in the following. This leads to the final formula for the field shift:

$$\delta E_{\mathrm{FS}}^{A,A'} = F \, \delta \left\langle r^2 \right\rangle^{A,A'}. \tag{6.21}$$

Total shift

Using the calculated expressions for the field and the mass shifts a more complete version of Eq. (6.1) is obtained:

$$\begin{aligned} \delta \nu^{A,A'} &= \delta \nu_{\mathrm{MS}}^{A,A'} + \delta \nu_{\mathrm{FS}}^{A,A'} \\ \delta \nu^{A,A'} &= (M_{\mathrm{SMS}} + M_{\mathrm{NMS}}) \frac{A - A'}{A A'} + F \, \delta \left\langle r^2 \right\rangle^{A,A'} \\ &= \left(M_{\mathrm{SMS}} + \nu_\infty \frac{m_{\mathrm{e}}}{m_{\mathrm{u}}} \right) \frac{A - A'}{A A'} + F \, \delta \left\langle r^2 \right\rangle^{A,A'}. \end{aligned} \tag{6.22}$$

6.2 Measurements and results

For the analysis of the isotope shift of the dipole transition in Os^-, the transition frequency was measured for all naturally occurring isotopes. Due to the high sensitivity of the collinear spectroscopy, also $^{184}Os^-$ was found, which is not visible in the mass spectra (e.g. Fig. 3.4), due to its low natural abundance of only 0.02% (compared to 1.58% of $^{186}Os^-$, the next rarest isotope).

From the measured data the rest frame frequencies (Tab. 6.1) were calculated using the transition in ^{192}Os as a reference and thereby deducing the shift of the measured frequencies. Figure 6.1 shows an overview over the measured transition frequencies in all isotopes, including the hyperfine structure of $^{187}Os^-$ and $^{189}Os^-$. Except for $^{187}Os^-$ and $^{189}Os^-$ the resonance frequencies follow a linear trend. The effect of separate linear trends amongst isotopes with even and odd mass numbers is called "even–odd staggering". This is due to the fact that the increase in nuclear radius is not proportional to the number of added neutrons – it is much larger when one neutron is added to an isotope with even mass number compared to half of the change in the nuclear radius when two neutrons are added.

In $^{187}Os^-$ and $^{189}Os^-$ the transition frequency is split due to the hyperfine structure (Chap. 5), therefore the center of gravity frequencies of the multiplets (Tab. 5.2) were used to calculate the shifts. As described in Chap. 5 the uncertainty of the absolute resonance frequencies of 35 MHz is mainly an error of the absolute value and only to a lesser extend an error of relative frequency measurements. Hence the uncertainty of the shifts is smaller than the one indicated from the errors of the single resonances. To rule out a drift of the frequency scale applied by the wavemeter, which could cause a relative error, several reference point measurements of the resonance frequency in $^{192}Os^-$ were done during the measurements on the different isotopes. The reference values had variations below 5 MHz. Therefore a total uncertainty of the shifts of 15 MHz, including the statistical uncertainty is reasonable. Since the resonances are distributed over a larger frequency interval than in case of the hyperfine structure the uncertainty is in this case bigger than described in Chap. 5.

In some studies on isotope shifts the measured shift is used to determine changes in the mean square nuclear radii $\delta \langle r^2 \rangle^{A,A'}$ between the different isotopes. For such an analysis, data for at least two different resonance frequencies are needed [19]. With the used laser system it is only possible to investigate one of the transitions in Os^-, preventing a determination of the $\delta \langle r^2 \rangle^{A,A'}$. However, since the changes in the nuclear radii of different isotopes are only an attribute of the nucleus itself and not affected by the electron shell structure, they are the same for the neutral osmium atom and the negative ion and experimental values are already available, e.g. from Ref. [19] (Tab. 6.1). Using these values it is possible to determine the FS coefficient F and the SMS coefficient M_{SMS} from the measured isotope shifts. As shown in Sec. 6.1, both shifts are related to the electron wavefunction and can

Tab. 6.1: Transition frequencies, isotope shifts and changes in mean square radii of the miscellaneous osmium isotopes with respect to $^{192}Os^-$. For $^{189}Os^-$ and $^{187}Os^-$ the center of gravity frequency is given. The values for $\delta\langle r^2\rangle$ are experimental results taken from [32].

Isotope	**transition freq(MHz)**	**Shift $\delta\nu^{192,A'}$(MHz)**	**$\delta\langle r^2\rangle^{192,A'}$(fm^2)**
$^{192}Os^-$	257 831 190(35)	0	0
$^{190}Os^-$	257 830 298(35)	-892(15)	-0.063(6)
$^{189}Os^-$	257 829 617(35)	-1573(15)	-0.111(11)
$^{188}Os^-$	257 829 285(35)	-1905(15)	-0.134(10)
$^{187}Os^-$	257 828 418(35)	-2772(15)	-0.191(14)
$^{186}Os^-$	257 828 070(35)	-3120(15)	-0.215(13)
$^{184}Os^-$	257 826 880(35)	-4310(15)	-0.298(17)

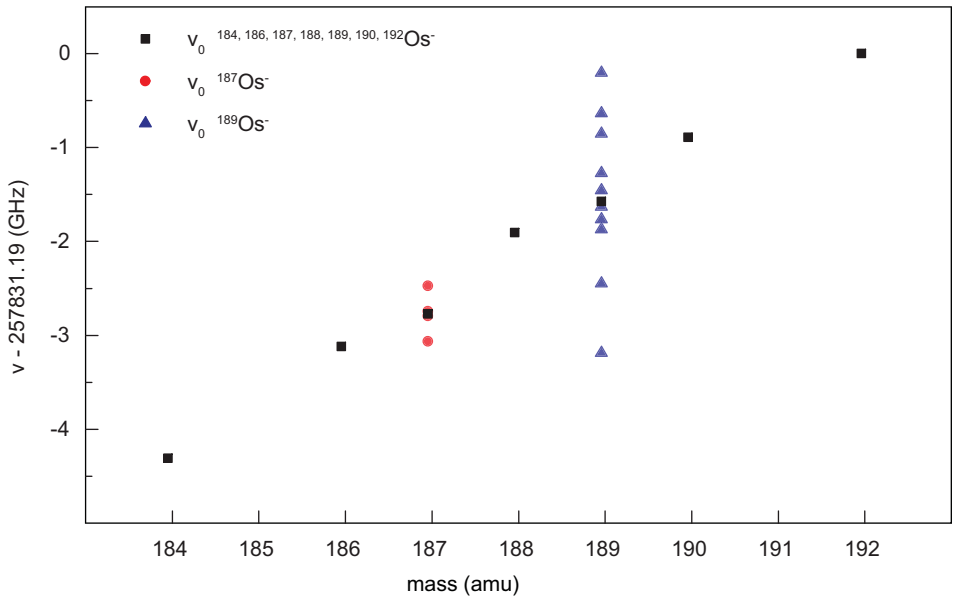

Fig. 6.1: Resonant transition frequencies of all measured isotopes and the calculated center of gravity frequencies of the hyperfine structure of $^{187}Os^-$ and $^{189}Os^-$. The origin of the ordinate is the resonance frequency of $^{192}Os^-$.

therefore be used to study the characteristics of the excess electron in the negative ion.

Since it contains all relevant constants including the measured isotope shifts $\delta\nu_{\mathrm{res}}^{A,A'}$, Eq. (6.22) is used for the analysis of the isotope shift. Subtraction of the NMS [Eq. (6.14)] from the total isotope shift $\delta\nu^{A,A'}$ leads to:

$$\begin{aligned} \delta\nu^{A,A'} &= (M_{\mathrm{SMS}} + M_{\mathrm{NMS}})\,\frac{A-A'}{AA'} + F\,\delta\left\langle r^2\right\rangle^{A,A'} \\ \delta\nu^{A,A'} - M_{\mathrm{NMS}}\frac{A-A'}{AA'} &= M_{\mathrm{SMS}}\frac{A-A'}{AA'} + F\,\delta\left\langle r^2\right\rangle^{A,A'}. \end{aligned} \tag{6.23}$$

Defining $\delta\nu_{\mathrm{res}}^{A,A'} = \delta\nu^{A,A'} - M_{\mathrm{NMS}}\,(A-A')\,/AA'$ in Eq. (6.23) as the residual isotope shift one finds:

$$\delta\nu_{\mathrm{res}}^{A,A'} = M_{\mathrm{SMS}}\frac{A-A'}{AA'} + F\,\delta\left\langle r^2\right\rangle^{A,A'}. \tag{6.24}$$

Finally multiplication of Eq. (6.24) by the factor $AA'/(A-A')$ gives:

$$\delta\nu_{\mathrm{res}}^{A,A'}\frac{AA'}{A-A'} = M_{\mathrm{SMS}} + F\cdot\left(\delta\left\langle r^2\right\rangle^{A,A'}\frac{AA'}{A-A'}\right), \tag{6.25}$$

which is a linear equation, with the FS coefficient F being the slope and the SMS coefficient M_{SMS} being the y intercept of the line. In Sec. 6.1 the NMS coefficient was defined as $M_{\mathrm{NMS}} = \nu_\infty m_{\mathrm{e}}/m_{\mathrm{u}}$. The resonance frequency ν_∞ of the fictitious isotope with infinite mass can be estimated using Eq. (6.6):

$$\nu_\infty = \frac{m_{\mathrm{e}}}{\mu_{\,^{192}\mathrm{Os}}}\,\nu_{^{192}\mathrm{Os}^-} \approx \nu_{^{192}\mathrm{Os}^-}. \tag{6.26}$$

This allows the calculation of M_{NMS} ($M_{\mathrm{NMS}} = 141.44$ GHz amu) and in combination with the measured shifts the determination of the residual isotope shifts $\delta\nu_{\mathrm{res}}^{A,A'}$.

Therefore F and M_{SMS} are the only unknown parameters of Eq. (6.25) and it is possible to determine them from a linear fit. Figure 6.2 shows the left-hand side of Eq. (6.25) as a function of $\delta\left\langle r^2\right\rangle^{192,A'} 192A'/\,(192-A')$. The large error bars in x direction originate from the uncertainty of the $\delta\left\langle r^2\right\rangle^{192,A'}$ of roughly 10%. The solid red line is a weighted linear regression fit, and the dashed brown curves show the uncertainty of the fit. The values of F and M_{SMS}, derived from the fit are given in Tab. 6.2. The FS is of the order of 1 GHz and the MS approximately one order of magnitude smaller. Since osmium belongs to the heavier elements this is exactly the behavior one would expect on the basis of the explanation given in the introduction to this chapter.

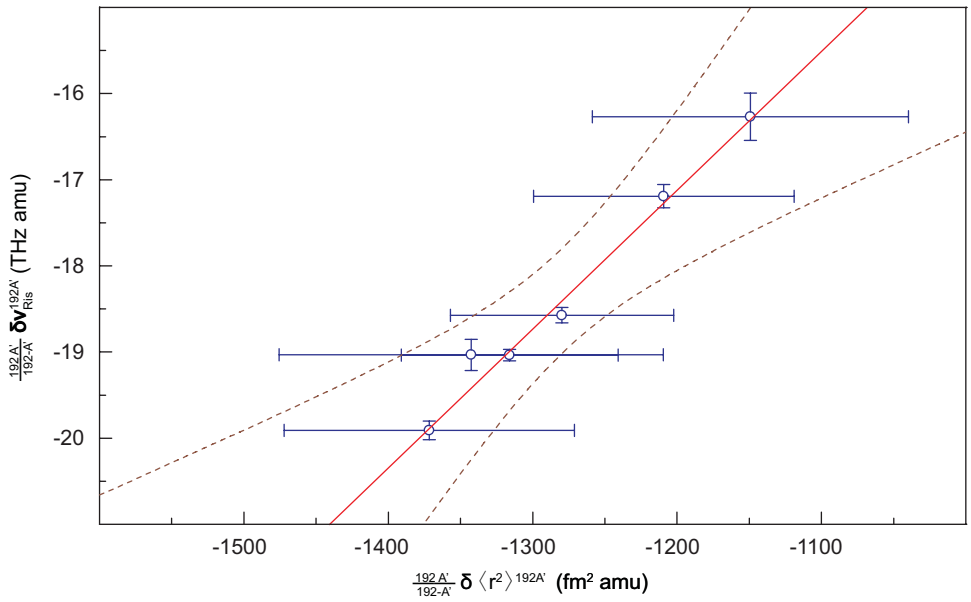

Fig. 6.2: Plot of $\nu_{\mathrm{res}}^{192,A'} 192A'/(192-A')$ as a function of $\delta\langle r^2\rangle^{192,A'} 192A'/(192-A')$. The solid red line is the weighted linear regression fit used for the determination of F and M_{SMS}, and the dashed brown lines show the uncertainty of the fit.

Tab. 6.2: The FS and the SMS coefficient of the E1 transition from $^4\mathrm{F}_{9/2}$ to $^6\mathrm{D}_{9/2}$ derived from the weighted linear regression fit shown in Fig. 6.2.

F	M_{SMS}
16(41) GHz fm^{-2}	2(11) THz amu

7. CONCLUSION

In this diploma thesis the frequency of the dipole transition in $^{192}Os^-$ and its cross section, the hyperfine structure of the dipole transition in $^{187}Os^-$ and $^{189}Os^-$ and the isotope shift of the transition in all naturally occurring isotopes were determined.

The transition frequency was measured with a relative precision of 10^{-7} and is therefore the most precise study of any atomic transition in a negative ion so far. From the cross section the partial lifetime for decay to the ground state was calculated. With 3(1) ms the mean lifetime of this decay is relatively long, which has an impact on the use of Os^- for laser cooling. For efficient laser cooling it is necessary that the decay of excited electrons is spontaneous and not stimulated. Due to the long decay time in the case of Os^-, the cooling rate can not exceed some tens of Hz, which results in estimated cooling times of several minutes from 4 K to the Doppler temperature. In the magnetic field of a Penning trap, in which the laser cooling will be carried out, the spectral lines are split due to the Zeeman effect. Therefore the next milestone on the route to laser cooling will be the measurement of the Zeeman shift of the dipole transition in $^{192}Os^-$. The number of Zeeman components is determined by the total angular momentum of the split state. As determined in the hyperfine structure measurement the ground and the excited state of the dipole transition have the same total angular momentum, which results in a similar splitting of both states. Hence it is already clear that it will be impossible to find a closed cooling cycle with only one possible Zeeman component of the ground state for decay. Therefore repumping with a second laser or a sideband of the primary cooling laser will be necessary. The long lifetime of the excited state, the low binding energy of its bound excited state, and the need for repumping make Os^- not at all an ideal candidate for laser cooling. But since Os^- is the only known negative ion with a dipole transition, a further thorough study of the prospects for laser cooling with Os^- is justified.

The measurements of the hyperfine structure of the dipole transition in $^{187}Os^-$ and $^{189}Os^-$ yielded the hyperfine structure constants of the ground and the excited states of both isotopes. Two different sets of variables were determined from the experimental data. Based on theoretical calculations, the more plausible set of variables was determined. Currently new calculations are being carried out by a collaborating theorist. Since the calculations will also include the excited state of the transition in $^{189}Os^-$, they should provide stronger input for the choice of the correct variables.

Finally the isotope shift of the dipole transition was measured in all naturally occurring isotopes. Based on these measurements the isotope shift coefficients of the transition were

successfully determined. The results of the measurements of the hyperfine structure and the isotope shift of the dipole transition in Os^- and the new theoretical results on the hyperfine splitting will soon be published in a combined experimental and theoretical paper.

A. ADDITIONAL MATERIAL FOR THE HFS MEASUREMENT

A.1 Intensities of HFS transitions

The relative intensities of HFS-components can be derived from equations given in the book of Condon and Shortley [30]. They were first derived by Kronig [36], Russel [37], Sommerfeld and Hönl [38] by the aid of the correspondence principle. The strengths of the spectral lines are calculated using the expectation value of the E1-operator P for two states with different parity. The formulas in the book describe intensities of transitions between fine structure multiplets in case of LS-coupling (Sec. 5.1), using the quantum numbers J, L and S. The formulas can also be applied to hyperfine structure. In this case J has to be replaced by F, L by J and S by I [36]. For transitions from a ground state multiplet with total angular momentum F to an excited state multiplett with $F^{'} = F - 1$ follows:

$$S\left(\gamma, I, J, F; \gamma^{'}, I, J-1, F+1\right) \propto (-1)^2 \, \tfrac{(F+I-J+1)(J+I-F)(F+I-J+2)(J+I-F-1)}{4(F+1)} \tag{A.1a}$$

$$S\left(\gamma, I, J, F; \gamma^{'}, I, J-1, F\right) \propto (2F+1) \, \tfrac{(F+J-I)(F+I-J+1)(I+J+1+F)(I+J-F)}{4F(F+1)} \tag{A.1b}$$

$$S\left(\gamma, I, J, F; \gamma^{'}, I, J-1, F-1\right) \propto \tfrac{(F+J-I-1)(F+J-I)(I+J+F+1)(I+J+F)}{4F} \tag{A.1c}$$

And for transitions from a multiplet with F to a multiplett with $F^{'} = F$:

$$S\left(\gamma, I, J, F; \gamma^{'}, I, J, F+1\right) \propto (-1)^2 \, \tfrac{(F-I+J+1)(F+I-J+1)(I+J+F+2)(J+I-F)}{4(F+1)} \tag{A.2a}$$

$$S\left(\gamma, I, J, F; \gamma^{'}, I, J, F\right) \propto (2F+1) \, \tfrac{[F(F+1)-I(I+1)+J(J+1)]^2}{4F(F+1)} \tag{A.2b}$$

$$S\left(\gamma, I, J, F; \gamma^{'}, I, J, F-1\right) \propto \tfrac{(F-I+J)(F+I-J)(I+J+F+1)(I+J+1-F)}{4F} \tag{A.2c}$$

A.2 Energy level diagrams of $^{187}Os^-$ and $^{189}Os^-$

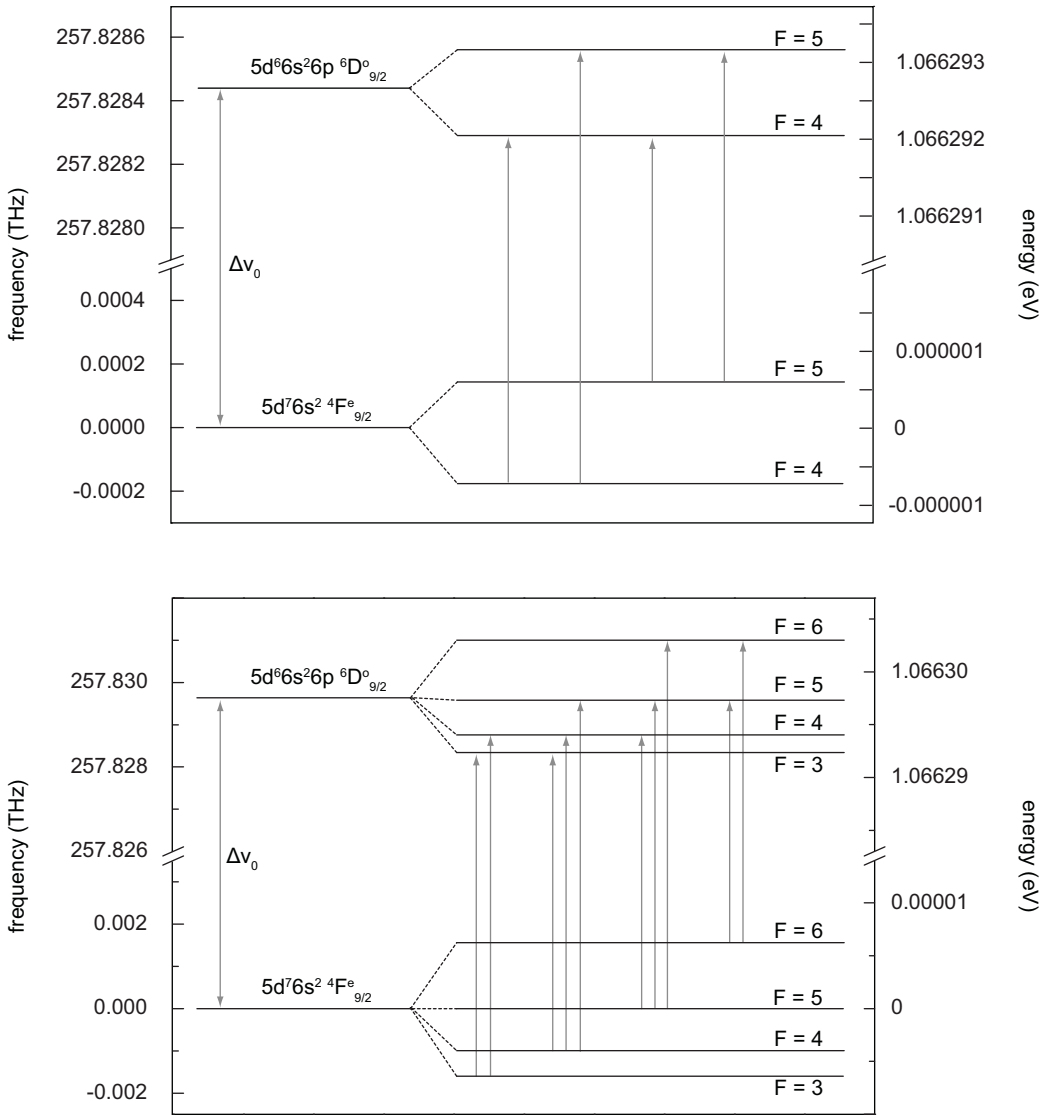

Fig. A.1: Upper graph: energy level diagram of $^{187}Os^-$. Lower graph: energy level diagram of $^{189}Os^-$. ν_0 is the center of gravity frequency of the hyperfine spectra. The splitting was calculated using the HFS constants A and B presented in Tab. 5.4.

B. ARTICLE

BIBLIOGRAPHY

[1] H. Hotop and W. C. Lineberger, J. Phys. Chem. Ref. Data **14**, 731 (1985).

[2] T. Anderson, H. K. Haugen, and H. Hotop, J. Phys. Chem. Ref. Data **28**, 1511 (1999).

[3] S. H. Vosko *et al.*, Phys. Rev. A **43**, 6389 (1991).

[4] D. Datta and D. R. Beck, Phys. Rev. A **50**, 1107 (1994).

[5] K. Dinov, D. R. Beck, and D. Datta, Phys. Rev. A **50**, 1144 (1994).

[6] S. M. O'Malley and D. R. Beck, Phys. Rev. A **78**, 012510 (2008).

[7] C. H. Greene, Phys. Rev. A **42**, 1405 (1990).

[8] J. L. Krause and R. S. Berry, in *18th Conf. At. Mol. Phys.*, p. 91, 1986, Comments.

[9] C. Froese Fischer and D. Chen, J. Mol. Struct. **199**, 61 (1989).

[10] A. M. Covington *et al.*, J. Phys. B **31**, L855 (1998).

[11] M. Scheer *et al.*, Phys. Rev. Lett. **80**, 684 (1998).

[12] R. C. Bilodeau and H. K. Haugen, Phys. Rev. Lett. **85**, 534 (2000).

[13] P. L. Norquist and D. R. Beck, Phys. Rev. A **61**, 014501 (1999).

[14] H. Massey, *Negative Ions*, 3rd ed. (Cambridge Univ. Press, 1976).

[15] J. Geddes *et al.*, J. Phys. B. **14**, 4837 (1981).

[16] J. Poulsen *et al.*, J. Phys. B. **23**, 457 (1990).

[17] N. Andersen *et al.*, J. Phys. B **17**, 2281 (1984).

[18] A. Kellerbauer and J. Walz, New J. Phys. **8**, 45 (2006).

[19] S. L. Kaufman, Opt. Commun. **17**, 309 (1976).

[20] R. Middleton, Nucl. Instrum. Methods **214**, 139 (1983).

[21] J. Meier, Matching of the beam from a negative-ion source for capture in a penning trap, Master's thesis, University of Heidelberg, 2007.

[22] U. Warring *et al.*, Phys. Rev. Lett. **102**, 043001 (2009).

[23] H. Haken and H. C. Wolf, *The Physics of Atoms and Quanta*, 5th edition ed. (Springer, Berlin, 1996).

[24] W. Demtröder, *Experimentalphysik 3*, 3rd ed. (Springer, Berlin, 2005).

[25] H. Kopfermann, *Kernmomente*, 2nd ed. (Akademische Verlagsgesellschaft M.B.H., Frankfurt am Main, 1956).

[26] H. Schüler and T. Schmidt, Zeitschrift für Physik **94**, 457 (1935).

[27] H. Casimir, Physica **2**, 719 (1935).

[28] H. G. Kuhn, *Atomic Spectra*, 2nd ed. (Longman Group Limited, 1969).

[29] W. C. Griffith *et al.*, Phys. Rev. Lett. **102**, 101601 (2009).

[30] E. U. Condon and G. H. Shortley, *The Theory of Atomic Spectra*, 5st ed. (Cambridge Univ. Press, 1959).

[31] A. Schwenk and G. Zimmermann, Phys. Lett. A **26**, 258 (1968).

[32] P. Aufmuth *et al.*, At. Data and Nucl. Data Tables **37**, 455 (1987).

[33] G. K. Woodgate, *Elemantary Atomic Structure*, 2nd ed. (Oxford University Press, 1989).

[34] K. Heilig and A. Steudel, At. Data and Nucl. Data Tables **14**, 613 (1974).

[35] E. C. Seltzer, Phys. Rev. **188**, 1916 (1969).

[36] R. d. L. Kronig, Z. Physik **33**, 261 (1925).

[37] H. N. Russell, Nature **115**, 835 (1925).

[38] A. Sommerfeld and H. Hönl, Sitz. der Preuss. Akad. d. Wiss. **9**, 141 (1925).

ACKNOWLEDGMENTS

With the last sentences of this thesis I want to mention those people who accompanied me during the last year.

First of all I want to thank Alban Kellerbauer who gave me the opportunity for an interesting and inspiring work in his group at the Max Planck Institute for Nuclear Physics in Heidelberg. Being under lots of stress in the end of my time at the MPI-K he managed anyway to have always enough time for questions, discussions and joint coffee breaks.

I want to thank my small group at the MPI-K, namely Carlo Canali and Ulrich Warring for the good collaboration and their friendship. In particular I have to thank my officemate Ulrich for numberless discussions and help whenever I needed a second opinion and Carlo for lots of funny tours on the MTB, which will hopefully go on. In this context also Oliver Herrwerth has to be mentioned as a good friend and companion on many "recreative" coursings in the Odenwald.

Special thanks go to Jasmin who was always there for me in the last years. And finally I want to thank my parents who made this thesis possible in first place. They early awakened my interest in natural sciences, laid thereby the cornerstone of my diploma in physics and support me whenever they can. At home are always an opened door and a warm welcome waiting for me.

ERKLÄRUNG:

Ich versichere, dass ich diese Arbeit selbstständig verfasst und keine anderen als die angegebenen Quellen und Hilfsmittel benutzt habe.

Heidelberg, den 01.04.2009